Research Square

Preprints are preliminary reports that have not undergone peer review.
They should not be considered conclusive, used to inform clinical practice,
or referenced by the media as validated information.

Electro–elastic–thermal coupling in electroosmotic transport of viscoelastic fluids: Steric-induced elastic stress restructuring and heat transfer regulation

Kuanhong Peng
Wuhan University of Technology
Weicheng Yu
Wuhan University of Technology
Yifei Sun
Wuhan University of Technology
Jie Li
jieli@whut.edu.cn

Wuhan University of Technology

Research Article

Keywords: Electroosmosis, Viscoelastic fluid, Thermal response, Steric constraint, Velocity slip

Posted Date: November 13th, 2026

DOI: https://doi.org/10.21203/rs.3.rs-11528665/v1

License: This work is licensed under a Creative Commons Attribution 4.0 International License.
Read Full License

Additional Declarations: No competing interests reported.

Electro–elastic–thermal coupling in electroosmotic transport of visco-elastic fluids: Steric-induced elastic stress restructuring and heat transfer regulation

Kuanhong Peng, Weicheng Yu, Yifei Sun, Jie Li*

School of Naval Architecture, Ocean and Energy Power Engineering, Wuhan University of Technology, Wuhan 430063, China;

Email addresses: 1287514347@qq.com (Kuanhong Peng); yuweicheng@whut.edu.cn (Weicheng Yu); 578516682@qq.com (Yifei Sun)

*Corresponding author, Email address: jieli@whut.edu.cn (Jie Li); Postal address: No. 1178 Heping Avenue, Wuchang District, Wuhan 430063, China

Abstract

Electroosmotic flow (EOF) is a fundamental actuation mechanism in microfluidic systems, where coupled electrokinetic and thermo-hydrodynamic processes govern microscale heat transfer. Under high surface potentials, steric effects and interfacial slip alter the electric double layer (EDL) structure and near-wall transport. In viscoelastic fluids, these interfacial effects further modulate the evolution of polymeric elastic stresses, leading to transport behaviors that deviate markedly from Newtonian EOF. Here, we develop a thermo-electrohydrodynamic model for electroosmotic transport of simplified Phan–Thien–Tanner (sPTT) fluids, incorporating finite ion-size effects and Navier slip. The coupled influences of the steric factor v, Debye parameter κ, slip length L_s, solvent viscosity ratio β, extensibility parameter ϵDe^2, and Brinkman number Br on the flow and thermal fields are systematically investigated. The results reveal a previously unreported mechanism of steric-effect-induced elastic stress restructuring. Unlike Newtonian fluids, where steric effects primarily weaken the electroosmotic driving force through EDL modification, in sPTT fluids increasing v leads to a reduction in near-wall peak normal and shear stresses while broadening their spatial distribution toward the channel core. This stress redistribution modifies the effective viscosity through the constitutive stress function, thereby reshaping velocity and temperature fields. Consequently, distinct thermal behaviors emerge, including enhanced sensitivity of temperature and Nusselt number in the low-κ regime, reversal of the Nu–v response at sufficiently high Br, and slip-induced multi-stage enhancement of heat transfer. The combined action of steric effects and interfacial slip establishes a nonlinear competition

between convective transport and internal heat generation, producing thermal responses absent in Newtonian EOF systems.

Keywords: Electroosmosis; Viscoelastic fluid; Thermal response; Steric constraint; Velocity slip.

1. Introduction

Microfluidics, which enables the manipulation of minute fluid volumes within microscale confined geometries, plays an increasingly important role in biomedical diagnostics [1,2], chemical processing [3,4], and electronic cooling technologies [5,6]. Among various microfluidic actuation methods, electroosmotic flow (EOF) is particularly attractive because it can generate efficient fluid transport without moving mechanical parts. EOF arises from the interaction between an externally applied electric field and the electric double layer (EDL) adjacent to charged channel walls. The migration of excess counter-ions within the EDL transfers momentum to the bulk fluid through viscous coupling, producing a nearly plug-like flow profile with low hydrodynamic dispersion [9,10]. These advantages make EOF a fundamental transport mechanism in numerous microfluidic applications, including sample manipulation, separation, mixing, and biochemical analysis [3-2].

Thermal transport is a critical aspect of electroosmotic microflows because it directly affects both transport efficiency and device reliability. In microscale systems, the large surface-to-volume ratio and steep velocity and temperature gradients considerably amplify the coupling between fluid flow and heat transfer. Temperature variations can alter the physicochemical properties of biological and chemical samples, while also influencing interfacial phenomena such as nanobubble formation and stability. As a result, thermal management has become an essential consideration in the design of modern microfluidic devices. Unlike macroscale flows, microchannel transport is dominated by surface-driven effects, including electrokinetic forces, capillarity, and interfacial slip [4]. Under high electric fields, Joule heating becomes unavoidable and may substantially modify local fluid properties, particularly viscosity and electrical conductivity [13,14]. These changes, together with viscous dissipation and other internal heat-generation mechanisms, can significantly affect electroosmotic transport and heat transfer characteristics. Therefore, elucidating the coupled thermo-hydrodynamic behavior of EOFs is of both fundamental and practical importance for the development of efficient microfluidic and thermal-management technologies.

The classical no-slip boundary condition is generally valid for macroscopic flows but may become inadequate in microfluidic systems, where fluid–solid interactions can induce appreciable velocity slip at the interface. Such slip effects are particularly pronounced on hydrophobic or molecularly smooth surfaces and can be further enhanced through surface engineering or specialized coatings [15,16]. Consequently, hydrophobic materials such as polydimethylsiloxane (PDMS) and polymethyl methacrylate (PMMA) have been widely employed in microfluidic device fabrication to improve flow performance. In EOF, interfacial slip has attracted considerable attention because it directly influences momentum transfer within the EDL and consequently alters the overall flow characteristics. The Navier slip condition is commonly adopted to characterize this phenomenon. Existing studies have demonstrated that velocity slip can significantly enhance transport performance in microscale flows. For example, Jing et al. [17] theoretically investigated convective heat transfer in microchannels with charge-dependent slip boundaries and reported noticeable heat-transfer enhancement. Jing and Pan [18] further examined the effects of surface-charge-dependent slip on electroviscous behavior and convective heat transfer in pressure-driven microtube flows, showing that the presence of slip increases the Nusselt number (*Nu*). These findings collectively indicate that interfacial slip serves as an effective mechanism for regulating both hydrodynamic and thermal transport processes in microfluidic systems.

The electroosmotic driving force is directly determined by the charge distribution within the EDL. Classical electrokinetic theories are commonly based on the Poisson–Boltzmann (PB) equation, which assumes ions to be point charges. While this approximation remains valid under moderate electrostatic conditions, it becomes increasingly inaccurate at high surface potentials, where strong counterion accumulation occurs near charged walls and finite ion-size effects become significant [19-21]. To overcome this limitation, various modified PB models have been proposed by incorporating steric constraints associated with the finite volume occupied by ions [22-27]. Representative studies by Borukhov et al. [28] and Mukherjee et al. [29] demonstrated that steric effects limit ion crowding within the EDL and alter both potential and charge-density distributions. These modifications lead to substantial changes in electroosmotic forcing and consequently affect momentum and heat transport. Recent studies have extended the steric framework toward thermal transport, nanoconfinement, and energy conversion. Sujith et al. [30] showed for pure EOF with interfacial slip that the steric effect on

the average Nusselt number reverses at a critical Brinkman number, and that the resulting heat-transfer degradation can be mitigated by adjusting the slip length. Wu et al. [31] found that steric effects and surface-charge mobility compete in governing the electroosmotic velocity in graphene nanochannels, whereas Zhang et al. [32] reported that a larger steric factor progressively degrades the electrokinetic energy conversion efficiency of Jeffrey nanofluids in porous microchannels. These studies demonstrate that finite ion-size effects propagate beyond the EDL into macroscopic momentum, thermal, and energy-conversion characteristics. Therefore, steric effects have emerged as an important factor in the analysis of EOF under high-surface-potential conditions, particularly in micro- and nanoscale systems where confinement effects are pronounced.

Existing studies have demonstrated that steric effects and interfacial slip significantly influence electroosmotic transport, while Joule heating and viscous dissipation play important roles in microscale thermal management [33]. However, most of these studies have focused on Newtonian fluids. In practical microfluidic and biological systems, many working fluids exhibit pronounced viscoelasticity, including polymer solutions, blood, and extracellular matrices. Owing to the presence of elastic stresses in addition to viscous stresses, viscoelastic fluids display unique rheological characteristics such as normal stress differences, shear thinning, and elastic instabilities. These phenomena introduce additional coupling between electrokinetic forcing, momentum transport, and heat transfer, making the thermal behavior of viscoelastic EOF fundamentally different from that of their Newtonian counterparts. Despite their practical relevance, the combined influences of viscoelasticity, steric effects, and interfacial slip on electroosmotic heat transfer remain insufficiently understood.

In recent years, increasing attention has been devoted to heat transfer in non-Newtonian EOF. Under slip boundary conditions, interfacial slip can significantly modify both hydrodynamic and thermal transport characteristics: for power-law fluids, it enhances convective heat transfer and alters entropy generation behavior in microchannels [34,35], and the slip-modulated hydrodynamics of such flows has since been examined in detail over broad parameter ranges [36]. These findings suggest that interfacial slip can serve as an effective mechanism for regulating transport processes in microscale systems.

In parallel, the influence of finite ion-size (steric) effects on electroosmotic transport has also been extensively explored. By modifying the ionic distribution within the EDL, steric effects can substantially alter electroosmotic forcing and consequently

affect flow and heat transfer characteristics. At induced high zeta potentials, finite ion size has been examined in combination with the viscoelectric effect [25], while for power-law fluids Sanjay and Harikrishnan [4] systematically investigated the slip thermofluidics over wide ranges of surface potential and steric factor, and Dey et al. [24] demonstrated that increasing steric effects reduce the Nusselt number. More recently, Fadaei et al. [37] showed that the influence of steric effects on thermal transport becomes increasingly pronounced under weakened surface cooling conditions, and Liu et al. [38] quantified the accompanying heat-transfer and entropy-generation characteristics in curved nanochannels. For Newtonian EOF, with and without electromagnetic effects, interfacial slip has also been considered together with the steric factor [30]: critical Brinkman and Péclet numbers were identified at which the steric effect on the average Nusselt number reverses, and the steric-induced heat-transfer degradation was shown to be mitigable by adjusting the slip length.

Collectively, these studies indicate that both steric effects and interfacial slip play important roles in determining the thermal performance of non-Newtonian EOF. Despite these advances, existing thermal investigations have focused predominantly on Newtonian fluids or generalized Newtonian fluids such as power-law models. For viscoelastic EOF, early studies concentrated on momentum transport, and although thermal transport has recently been examined for viscoelastic fluids, including PTT and sPTT models **Error! Reference source not found.**-42], the ionic species have been treated as point charges throughout. Within the viscoelastic framework, only Mukherjee et al. [29] have incorporated finite ion size together with interfacial slip, and their analysis was restricted to the momentum field, without any consideration of heat transfer. In contrast, viscoelastic fluids possess an additional elastic stress field that can interact with electrokinetic forcing, interfacial slip, and ion-distribution dynamics, potentially introducing transport mechanisms that are absent in purely viscous fluids. In particular, under the combined influences of steric effects, interfacial slip, electroosmotic driving, Joule heating, and viscous-elastic dissipation, the coupling among EDL structure, elastic stress evolution, momentum transport, and heat transfer remains poorly understood. A systematic understanding of how microscale ionic redistribution propagates through elastic stress feedback to influence macroscopic thermal transport is still lacking.

To bridge this gap, this study develops a thermo-electro-hydrodynamic model for EOF of sPTT viscoelastic fluids by incorporating both steric effects and Navier slip boundary conditions. The coupled influences of finite ion-size effects, interfacial slip,

viscoelasticity, and thermal dissipation on flow and heat transfer characteristics are systematically investigated under constant wall heat-flux conditions. A central objective of this work is to uncover the mechanism of steric-effect-induced elastic stress restructuring and its role in thermal transport modulation. Unlike Newtonian EOF, where steric effects primarily alter the electroosmotic driving force through EDL modification, the present study demonstrates that steric effects can also restructure the spatial distribution of polymer elastic stresses. This stress redistribution propagates from the microscale EDL to the momentum and thermal transport processes, ultimately producing distinct heat-transfer responses. Based on these findings, a unified electro–elastic–thermal coupling framework is established, providing a new perspective for understanding and regulating heat transfer in complex-fluid microflows.

2. Mathematical Model

2.1 Geometric Model

The present study considers a two-dimensional, steady, laminar, and incompressible EOF of an sPTT viscoelastic fluid in a rectangular microchannel with height $2H$ and length L, as illustrated in Fig. 1. Owing to geometric and physical symmetry about the channel centerline, only the upper half of the computational domain is considered, thereby improving computational efficiency. A uniform electric field E is applied along the streamwise direction, while the channel walls are subjected to a constant heat flux q. The inlet fluid temperature is specified as T_i. The streamwise and transverse coordinates are denoted by x and y, respectively.

To facilitate the theoretical formulation, several commonly adopted assumptions are introduced: the EDLs do not overlap; the flow is considered to be hydrodynamically and thermally fully developed; the walls carry a uniform Zeta potential ζ^*; the convective transport of ions is negligible; and the electrolyte solution is assumed to be a symmetric binary electrolyte ($Z^+ = Z^- = Z$) with a bulk concentration c_0.

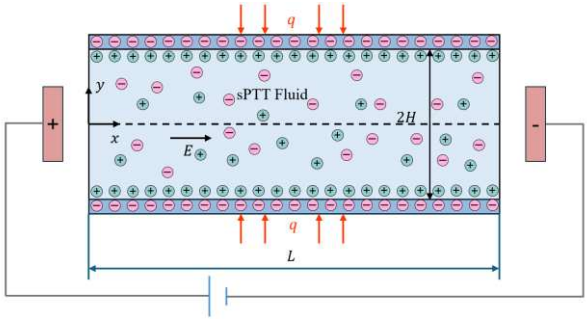


Fig. 1. Schematic diagram of the geometric model.

2.2 Governing Equations

The flow is governed by the incompressible continuity equation and the momentum equation. For a fully developed viscoelastic fluid flow, the Cauchy momentum equation incorporating the electroosmotic body force can be expressed as:

$$\nabla \cdot \boldsymbol{u} = 0 \tag{1}$$

$$-\nabla p + \nabla \cdot \boldsymbol{\tau} + \mu \nabla^2 \boldsymbol{u} + \rho_e \boldsymbol{E} = 0 \tag{2}$$

where $\boldsymbol{u}$ is the velocity vector, p is the pressure, $\boldsymbol{\tau}$ is the polymeric extra stress tensor, and μ is the solvent viscosity of the fluid. $\boldsymbol{E}$ is the electric field vector, and ρ_e represents the electric body force per unit volume arising from the applied electric field.

In EOF, the electric field acts along the axial direction. The charge density is obtained from the Poisson equation, which is derived from Gauss's law. This equation relates the charge density of the ionic solution to the electric potential (ψ) as follows:

$$\nabla^2 \psi = -\frac{\rho_e}{\varepsilon} \tag{3}$$

where $\varepsilon = \varepsilon_0 \varepsilon_r$ with ε_0=8.854$\times 10^{-12}$ F/m being the vacuum permittivity and ε_r is the relative permittivity of the solvent. The electric field $\boldsymbol{E}$ is related to the electric potential with $\boldsymbol{E} = -\nabla \psi$.

For a symmetric dilute electrolyte, the charge density is a function of the electric potential, and the relationship between them is given by the Boltzmann distribution:

$$\rho_e = -2 n_0 e z \sinh\left(\frac{ze\psi}{k_B T}\right) \tag{4}$$

Here, n_0 is the bulk ionic concentration, e is the elementary charge, z is the ionic valence, k_B is the Boltzmann constant, and T is the absolute temperature. Substituting Eq. (4) into Eq. (3) yields the Poisson–Boltzmann distribution for the charge density:

$$\nabla^2 \psi = \frac{2 n_0 e z \sinh\left(\frac{ze\psi}{k_B T}\right)}{\varepsilon} \tag{5}$$

To account for the effect of finite ion size, a steric factor ν is introduced, which characterizes the volume fraction of hydrated ions in the bulk. The electric potential distribution can then be expressed as:

$$\nabla^2 \psi = \frac{2 n_0 e z \sinh\left(\frac{ze\psi}{k_B T}\right)}{1 + 4\nu \sinh^2\left(\frac{ze\psi}{2 k_B T}\right)} \tag{6}$$

Introducing the dimensionless potential $\Psi = \frac{ze\psi}{k_B T}$, Eqs. (5) and (6) can be rewritten as:

$$\nabla^2\Psi = \frac{\kappa^2 \sinh(\Psi)}{1+4v\sinh^2(\frac{\Psi}{2})} \tag{7}$$

where $\kappa(=H/\lambda_D)$ denotes the Debye parameter, and $\lambda_D = (2n_0e^2z^2/\varepsilon k_BT)^{\frac{1}{2}}$ is the Debye length.

In this work, the sPTT model is employed to describe the rheological behavior of the viscoelastic fluid. The polymeric extra stress tensor τ is governed by:

$$f(\tau_{kk})\boldsymbol{\tau} + \lambda\overset{\nabla}{\boldsymbol{\tau}} = 2\eta_p\boldsymbol{D} \tag{8}$$

where $\boldsymbol{D} = (\nabla\boldsymbol{u} + \nabla\boldsymbol{u}^T)/2$ is the rate of deformation tensor. For the fluid, we define the zero-shear-rate total viscosity, η_0=η_p+η_s, where η_p is the polymer viscosity, and η_s is the solvent viscosity, with the coefficient $\beta = \eta_s/\eta_0$ is the viscosity ratio. The symbol $\overset{\nabla}{\boldsymbol{\tau}}$ represents the upper-convected derivative of the stress tensor $\boldsymbol{\tau}$, and λ denotes the relaxation time of the viscoelastic fluid. The expression for $\overset{\nabla}{\boldsymbol{\tau}}$ is given by:

$$\overset{\nabla}{\boldsymbol{\tau}} = \frac{D_{\boldsymbol{\tau}}}{D_t} - (\nabla\boldsymbol{u})^T\cdot\boldsymbol{\tau} - \boldsymbol{\tau}\cdot\nabla\boldsymbol{u} \tag{9}$$

For the sPTT model, the stress coefficient function $f(\tau_{kk})$ is defined as [43]:

$$f(\tau_{kk}) = 1 + \frac{\epsilon\lambda}{\eta_p}\tau_{kk} \tag{10}$$

where ϵ is the extensibility parameter, and $\tau_{kk} = \tau_{xx} + \tau_{yy} + \tau_{zz}$ is the trace of the extra stress tensor. As $\epsilon \to 0$, the model reduces to the upper-convected Maxwell (UCM) model, which is suitable for dilute polymer solutions. Invoking the assumptions of fully developed two-dimensional flow and unidirectional flow (u,0,0), and combining Eqs. (8)–(10), the following simplified relations are obtained for further analysis [44]:

$$f\big(\tau_{xx}+\tau_{yy}\big)\tau_{xx} = 2\lambda(\frac{du}{dy})\tau_{xy} \tag{11a}$$

$$f\big(\tau_{xx}+\tau_{yy}\big)\tau_{yy} = 0 \tag{11b}$$

$$f\big(\tau_{xx}+\tau_{yy}\big)\tau_{xy} = \eta_p\frac{du}{dy} + \lambda\frac{du}{dy}\tau_{yy} \tag{11c}$$

Setting $\tau_{yy} = 0$ in Eq. (11b) yields $\tau_{kk} = \tau_{xx}$. Dividing Eq. (11c) by Eq. (11a) then gives $\tau_{xx} = (2\lambda/\eta_p)(\tau_{xy})^2$. Substituting this result back and simplifying leads to the following shear stress relation:

$$\tau_{xy} + \frac{2\epsilon\lambda^2}{{\eta_p}^2}(\tau_{xy})^3 = \eta_p\frac{du}{dy} \tag{12}$$

Under fully developed conditions, the modified Cauchy momentum equation, Eq. (2), takes the form:

$$\frac{d\tau_{xy}}{dy} = \varepsilon E \frac{d^2\psi}{dy^2} \tag{13}$$

Integrating Eq. (13) and applying the symmetry boundary condition $(\psi, \tau_{xy})_{y=0} = 0$ yields:

$$\tau_{xy} = \varepsilon E \frac{d\psi}{dy} \tag{14}$$

Substituting Eq. (12) into Eq. (14) gives the analytical expression for the velocity gradient within the microchannel:

$$\frac{du}{dy} = \frac{\varepsilon E}{\eta_p}\frac{d\psi}{dy} + \frac{2\epsilon\lambda^2\varepsilon^3 E^3}{{\eta_p}^3}\left(\frac{d\psi}{dy}\right)^3 \tag{15}$$

To obtain the dimensionless form of the equations, the following scales are introduced: $X = x/L$, $Y = y/H$, $U = u/u_{hs}$, $De = \lambda\kappa u_{hs}/H$, and $\zeta = ze\zeta^*/k_BT$. The dimensionless velocity gradient then becomes:

$$\frac{dU}{dY} = -\frac{1}{\zeta}\frac{d\psi}{dy} - \frac{2\epsilon De^2}{\kappa^2\zeta^3}\left(\frac{d\Psi}{dY}\right)^3 \tag{16}$$

where $u_{hs} = -\varepsilon\zeta^* E/\eta_0$ is the Helmholtz–Smoluchowski velocity, and the Deborah number De represents the ratio of the fluid relaxation time to the characteristic flow time within the EDL, serving as a measure of the significance of viscoelastic effects.

In hydrophobic microfluidic systems, the no-slip boundary condition often leads to unrealistic predictions. To address this issue, the Navier-slip model [45] is adopted to account for interfacial slip. According to this model, the slip boundary condition at the wall is expressed as:

$$u_s = -\beta^* \frac{du}{dy} \tag{17}$$

where u_s is the slip velocity and β^* is the slip length. The dimensionless form of Eq. (17) is:

$$U_s = -L_s \frac{dU}{dY} \tag{18}$$

where $L_s(= \beta^*/H)$ is the dimensionless slip coefficient, and $U_s = u_s/u_{hs}$ is the dimensionless slip velocity.

To obtain the temperature field, the energy equation incorporating viscoelastic dissipation and volumetric heat generation is written as [46] :

$$\rho c_p(\boldsymbol{u}\cdot\nabla T) = k\nabla^2 T + \boldsymbol{\tau}\colon\nabla\boldsymbol{u} + \sigma(\boldsymbol{E}\cdot\boldsymbol{E}) \tag{19}$$

where ρ, c_p, T, k, and σ are the fluid density, specific heat capacity, temperature, thermal conductivity, and electrical conductivity, respectively. The term $\tau\colon\nabla u$ represents the rate of mechanical work per unit volume. In viscoelastic fluids, this work is

generally partitioned between reversible elastic energy storage and irreversible dissipation. However, under the steady, fully developed flow conditions considered in this work ($\partial/\partial t = 0,\ \partial/\partial x = 0$), the elastic energy storage rate along a streamline vanishes identically. Consequently, the mechanical work $\tau : \nabla u$is entirely converted to irreversible heat, and may be referred to as the viscoelastic dissipation heat generation throughout this paper.

Introducing the dimensionless temperature $\theta = (T - T_i)k/Hq$ and the dimensionless shear stress $\tau_{xy}^* = \tau_{xy}H/\eta_0 u_{hs}$, and defining the Péclet number $Pe = \rho c_p u_{hs} H/k$, the Brinkman number $Br = \eta u_{hs}^2/qH$, and the Joule heating parameter $G = \sigma E_x^2 H/q$, the dimensionless form of Eq. (19) is obtained as:

$$Pe(U \cdot \nabla\theta) = \nabla^2\theta + Br \cdot \Phi + G \tag{20}$$

where $\Phi = \tau_{xy}^* \cdot dU/dY$ is the dimensionless dissipation function. Under the ionic concentration conditions considered in this work, $G \approx 0$, and the Joule heating term exerts no practical influence on the temperature field.

The heat transfer performance in the microchannel is quantified by the Nusselt number, defined as:

$$Nu = \frac{hH}{k} \tag{21}$$

where $h = q/(T_w - T_m)$ is the heat transfer coefficient, and T_w and T_m are the wall temperature and the bulk mean temperature at any cross-section, respectively. In dimensionless form, the Nusselt number can be expressed as:

$$Nu = \frac{1}{(\theta_w - \theta_m)} \tag{22}$$

The dimensionless bulk mean temperature is calculated as:

$$\theta_m = \frac{\int_0^1 U\theta dY}{\int_0^1 U dY} \tag{23}$$

2.3 Physical Parameters

The numerical ranges and physical parameters employed in the present study are summarized in Table 1.

Table 1. Numerical ranges and physical parameters employed in the present study.

Symbol	Name	Value	Unit
L	Microchannel length	1000	μm
H	Microchannel half-height	10	μm
ρ	Density	1000	kg/m^3
η	Fluid viscosity	0.001	kg/(m·s)

β	Solvent viscosity ratio	0.1~0.6	-
ε	Solution permittivity	7.0124×10^{-10}	F/m
k_B	Boltzmann constant	1.381×10^{-23}	J/K
e	Elementary charge	1.602×10^{-19}	C
z	Ionic valence	±1	-
E	Applied electric field strength	10000	V/m
T	Initial fluid temperature	300	K
ζ^*	Zeta potential	-100	mV
κ	Debye parameter	5~30	-
ϵDe^2	Viscoelastic extensibility parameter	0~2	-
L_s	Slip coefficient	0~0.1	-
v	Steric factor	0~0.3	-
Br	Brinkman number	10^{-9}~10^{-1}	-
Pe	Péclet number	0~0.1	-

2.4 Boundary Conditions

The boundary conditions associated with the governing equations are as folow：

at the wall $(Y=1)$：$\Psi=\zeta$，$U=U_s$，$\frac{\partial\theta}{\partial Y}=1$

at the center $(Y=0)$：$\frac{d\Psi}{dY}=0$，$\frac{dU}{dY}=0$，$\frac{\partial\theta}{\partial Y}=0$

at the inlet ：$\frac{d\Psi}{dX}=0$，$\theta=0$

at the outlet ：$\frac{d\Psi}{dX}=0$，$\frac{\partial\theta}{\partial X}=0$

3. Grid Independence and Numerical Method Validation

3.1 Solver Overview

Numerical simulations in this study are performed using the rheoHeatFoam solver within the open-source viscoelastic fluid toolbox **rheoTool** (version 6.0), which is built upon the finite-volume computational platform **OpenFOAM®** (version 9.0). To enhance the numerical stability of viscoelastic flow calculations, the solver incorporates the both-side diffusion (BSD) technique. The temporal derivative is discretized using a first-order implicit Euler scheme; the gradient terms are discretized with a Gauss linear

scheme; the Laplacian terms are discretized with a Gauss linear corrected scheme incorporating non-orthogonal correction. For the convective terms, the divergence of the velocity field is treated with a no-convection scheme (GaussDefCmpw none), while the convective parts of scalar transport quantities such as temperature and polymer stress uniformly adopt the high-resolution cubic interpolation scheme (GaussDefCmpw cubista) to ensure accuracy while effectively suppressing numerical diffusion. The velocity–pressure coupling is handled via the SIMPLE algorithm. The pressure, velocity, and electric-potential-related variables are solved using a PCG solver with a DIC preconditioner, whereas the temperature, polymer stress, and related scalars are solved using a PBiCG solver with a DILU preconditioner.

3.2 Grid Independence Verification

To rigorously ensure the reliability of the numerical simulations, a systematic grid convergence analysis was carried out for the modified PB equation incorporating ionic steric effects. Owing to the steep electric potential gradients in the near-wall region, the model exhibits strong nonlinearity and is consequently highly sensitive to the grid resolution. Fig. 2a show the grid division in the vertical direction of the channel and within the double layer, respectively.Four levels of graded mesh (M1–M4) were employed, with the number of grid cells within the boundary layer set to 45, 60, 75, and 90, corresponding to total cell counts of 14,250, 25,000, 31,250, and 45,000, respectively. The grid expansion ratio was set to 0.2 inside the boundary layer and 0.4 in the remaining domain. Under the conditions of Debye parameter κ=5, steric factor ν=0.3, and slip coefficient L_s=0.1, the dimensionless velocity profiles along the Y-axis were extracted (see Fig. 2b). The results show that the distributions for M2, M3, and M4 are in close agreement, whereas M1 exhibits a noticeable deviation. Quantitative analysis indicates that, relative to the finest mesh M4, the relative errors of M1, M2, and M3 are 1.54%, 0.59%, and 0.70%, respectively. Balancing accuracy (error < 1%) against computational cost, M2 satisfies the accuracy requirement while reducing the computational effort by approximately 50% compared with M4. Accordingly, all subsequent simulations were performed using the M2 mesh.

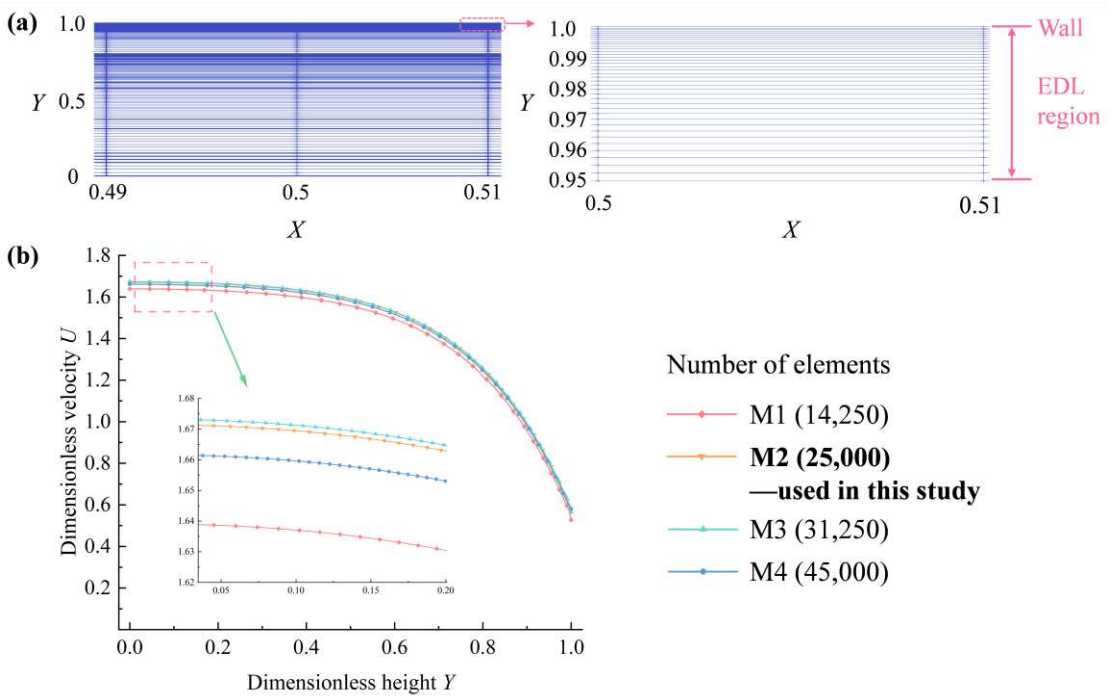


Fig. 2. (a) Mesh used in the vertical direction of the channel and the grid division in the EDL region; (b) Variation of the dimensionless velocity along the *Y*-direction under different meshes.

3.3 Numerical Method Validation

To validate the accuracy of the established model, the open-source software RheoTool was employed for the numerical solution, and the computed results were compared against those reported in the literature [33], as shown in Fig. 3. Two types of fluids were used for validation: the first was a Newtonian fluid, and the second was an sPTT fluid. The Newtonian fluid simulations were performed under the following conditions: Debye parameter κ=10, slip coefficient L_s=0.05, electric field strength E=10000 V/m, Zeta potential ζ^*=-100 mV, relative permittivity ε_r=77.232, density ρ=1000 kg/m^3, and viscosity μ=0.001 Pa·s. For the sPTT fluid, a relaxation time of 10^{-4} s and an extensibility parameter ϵ=10^{-4} were adopted, with all other parameters kept identical to those of the Newtonian case, so that the sPTT fluid closely approximates a Newtonian fluid. To verify the influence of the steric effect on the flow field, two cases with steric factors v=0.1 and v=0.3 were simulated, and the dimensionless velocity profiles along the transverse direction at the central cross-section were obtained, as presented in Fig. 3. The numerical results are in excellent agreement with the literature data, confirming the reliability and accuracy of the proposed model and solution methodology. In addition, it can be observed that the simulation results for the near-Newtonian sPTT fluid are essentially identical to those for the Newtonian fluid.

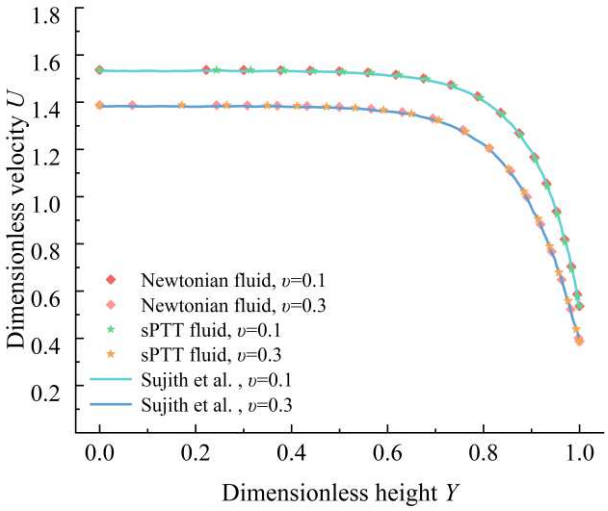


Fig. 3. Comparison of the present numerical results with those of Sujith et al. [33].

4.Results and Discussion

To systematically elucidate the underlying electro–elastic–thermal coupling mechanism, the subsequent analysis is organized into five interconnected levels: EDL restructuring, elastic stress redistribution, velocity-field reshaping, thermal boundary-layer response, and Nusselt number variation. This hierarchical framework enables the progressive identification of how microscale electrokinetic modifications propagate through momentum transport and ultimately influence macroscopic heat-transfer behavior.

For the representative conditions ($\epsilon De^2 = 1,\ \kappa = 20,\ \nu = 0.3$), Fig. 4 illustrates the axial evolution of the dimensionless velocity and temperature fields of the sPTT fluid. As the flow develops downstream, the electroosmotic body force rapidly approaches a streamwise-invariant distribution because both the applied electric field and wall surface charge remain uniform along the channel. Simultaneously, the polymer elastic stresses attain a steady spatial structure, resulting in a fully developed velocity profile that no longer varies with the dimensionless channel length X. Under the constant wall heat-flux condition, the dimensionless temperature increases linearly along the channel, exhibiting the characteristic behavior of thermally fully developed flow. In this regime, the cross-sectional temperature profile becomes self-similar, while the axial temperature gradient remains constant. Although viscoelastic dissipation acts as a distributed volumetric heat source, its magnitude becomes spatially invariant once the velocity and stress fields are fully developed. Consequently, it modifies only the value of the axial temperature gradient without altering the linear growth of temperature along

the channel. Based on these observations, the cross-section at $X = 0.5$ is selected as a representative location within the fully developed region for all subsequent analyses of the velocity, stress, and thermal fields. Furthermore, unless otherwise specified, the solvent-free limit (β=0) is adopted throughout the discussion to isolate and emphasize the influence of elastic effects on electroosmotic transport and heat transfer.

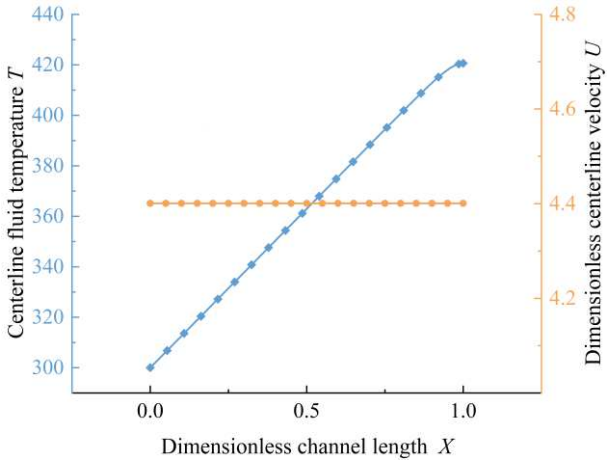


Fig. 4. Variation of the dimensionless centerline temperature with the dimensionless channel length X.

4.1 Steric-Effect-Induced Elastic Stress Redistribution

To clarify the origin of the observed stress response, the influence of steric hindrance on the EDL structure is first examined. Fig. 5 depicts the dimensionless electrostatic potential distributions along the wall-normal direction for different steric factor values. As the steric factor ν increases from 0 to 0.3, the magnitude of the near-wall potential becomes larger, while its decay toward the channel centerline becomes progressively slower. Consequently, the region over which the electrostatic potential remains significant extends further into the bulk fluid. Because the potential distribution is directly coupled to the ionic distribution within the EDL, these changes indicate that finite ion-size effects substantially alter the organization of ions near the charged wall. Rather than merely weakening electrostatic interactions, steric hindrance redistributes the ionic population within the EDL and broadens the charge-affected region. As a result, the originally concentrated EDL becomes increasingly diffuse, leading to a modified electrokinetic forcing structure. For EOF, the EDL determines the spatial distribution of the electroosmotic body force. Therefore, the steric-effect-induced modification of the EDL not only changes the magnitude of the driving force but also alters its wall-normal distribution. This redistribution directly affects the near-wall velocity gradient

and the stretching dynamics of polymer chains in the sPTT fluid. Through the coupling between flow kinematics and viscoelastic constitutive behavior, the altered polymer deformation field subsequently reshapes the elastic stress distribution. The following section therefore focuses on elucidating how EDL restructuring propagates to the elastic stress field and ultimately governs the observed stress response.

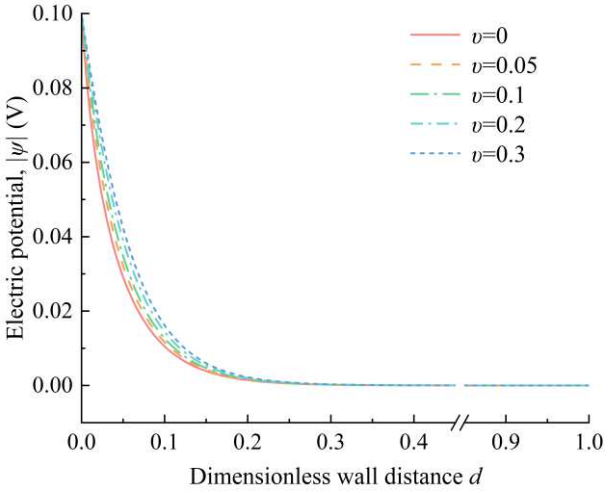


Fig. 5. Variation of the absolute electric potential of the sPTT fluid with the dimensionless near-wall distance d at $\epsilon De^2 = 1$, L_s=0.1, and κ=20.

Unlike Newtonian fluids, viscoelastic fluids are capable of storing and releasing elastic energy during flow. Consequently, their dynamics are governed not only by the electroosmotic body force but also by the elastic stress feedback generated through polymer stretching and shearing. Because the electroosmotic driving force is primarily confined within the EDL, the generation of polymer stresses is likewise highly localized near the wall. The extent of this localization is determined by the Debye parameter κ: for κ=20, the characteristic EDL thickness is approximately 5% of the channel half-height, whereas for κ=10 it increases to about 10%. Regardless of whether the system is regulated through the steric factor ν or the solvent viscosity ratio β, the electroosmotic forcing and the resulting polymer deformation remain concentrated within this narrow near-wall region. This common origin explains the highly localized nature of all stress variations observed in the present study.

To isolate the effect of steric hindrance on the elastic stress field, Fig. 6 first examines the distributions of the polymeric normal stress τ_{xx} and shear stress τ_{xy} under different steric factors at κ=20. As shown in Fig. 6a, increasing ν from 0 to 0.3 causes the peak normal stress near the wall to decrease dramatically from approximately 240 Pa to 50 Pa, corresponding to a reduction of nearly 80%. Simultaneously,

the stress decay becomes progressively more gradual and the region influenced by elastic stresses extends farther toward the channel interior. This behavior originates from the finite ion-size effect: steric hindrance restricts the accumulation of counter-ions adjacent to the wall, thereby reducing the local charge density and weakening the electroosmotic body force. The resulting decrease in velocity gradients suppresses polymer stretching, and the nonlinear extensional response inherent in the sPTT constitutive model further amplifies this attenuation. Consequently, the stored elastic energy is reduced and redistributed over a broader spatial region.

A similar trend is observed for the polymeric shear stress in Fig. 6b. Although the peak magnitude of $|\tau_{xy}|$ decreases with increasing ν, the more important feature is the migration of the active shear region. Within the immediate vicinity of the wall ($d <$ 0.02), the shear stress is greater for lower steric factors; however, beyond approximately $d \approx 0.02$, the stress associated with larger ν becomes dominant. This crossover behavior indicates that steric hindrance does not simply weaken shear stresses uniformly. Instead, it redistributes the zone of intense shear action away from the wall and toward the outer edge of the EDL. As ion crowding is suppressed, the charge distribution becomes slightly broader, leading to a corresponding redistribution of the electroosmotic forcing and velocity gradients required by momentum balance.

A key observation emerging from Fig. 6 is that both the normal-stress and shear-stress curves intersect at approximately $d \approx 0.02$. On the wall side of this location, lower steric factors produce larger stresses, whereas farther from the wall the trend reverses. Such crossover behavior provides direct evidence that steric hindrance fundamentally alters the spatial organization of the elastic stress field. Increasing ν simultaneously suppresses the peak stress level and broadens the region over which elastic stresses remain active. Consequently, the stress field evolves from a highly concentrated, high-intensity structure into a more diffuse, lower-intensity configuration.

These results demonstrate that the primary role of steric hindrance in viscoelastic EOF is not merely to attenuate elastic stresses, but rather to restructure their spatial distribution. This steric-effect-induced elastic stress restructuring constitutes the second stage of the electro–elastic–thermal coupling pathway established in this work, linking EDL modification to subsequent velocity-field reshaping and nonlinear thermal transport behavior.

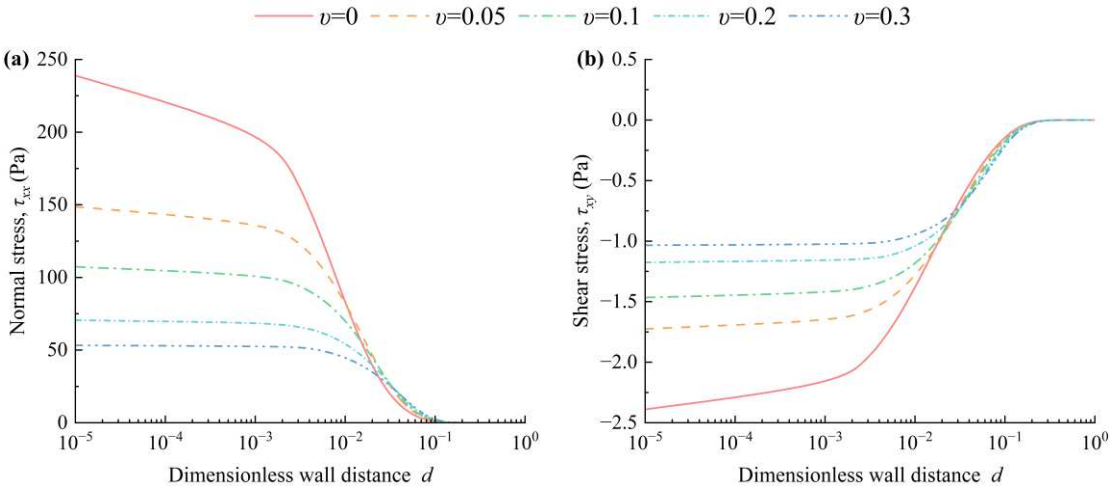


Fig. 6. Variation of the normal stress τ_{xx} (a) and shear stress τ_{xy} (b) of the sPTT fluid with the dimensionless near-wall distance d under different steric factors ν at $\epsilon De^2 = 1$, L_s=0.1, and κ=20.

Fig. 7 presents the distributions of τ_{xx} and τ_{xy} under the fixed conditions of ν=0.2 and κ=10 for various solvent viscosity ratios β. In sharp contrast to the curve crossover and stress-action-zone broadening induced by increasing ν in Fig. 6, both τ_{xx} in Fig. 7a and τ_{xy} in Fig. 7b decrease monotonically as β increases. The stress profiles preserve the same ordering across the entire wall-normal direction, exhibiting neither curve intersection nor any noticeable variation in the width of the stress-action region.

As shown in Fig. 7a, the near-wall peak value of τ_{xx} decreases from approximately 12.8 Pa to 3.5 Pa, corresponding to a reduction of more than 70%. Similarly, the peak value of τ_{xy} in Fig. 7b decreases by about 65%. The stronger attenuation of the normal stress compared with the shear stress originates from their different dependencies on the velocity gradient in the constitutive equation. Specifically, the normal stress is amplified through nonlinear elastic stretching and therefore exhibits a stronger sensitivity to the reduction of the polymeric contribution, whereas the shear stress retains a direct linear dependence on the local velocity gradient and consequently decreases more moderately. These results demonstrate that increasing β primarily acts to dilute the polymeric elastic contribution to the total stress. As a result, the elastic stress field undergoes a nearly uniform attenuation throughout the channel, reducing the stress magnitude while leaving the overall spatial distribution and stress-action-zone width essentially unchanged.

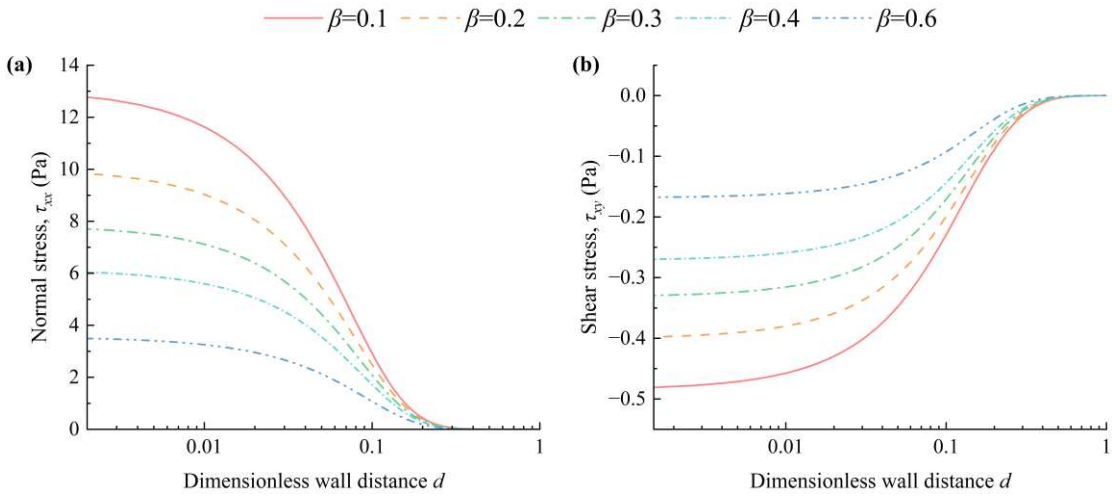


Fig. 7. Variation of the normal stress τ_{xx} (a) and shear stress τ_{xy} of the sPTT fluid with the dimensionless near-wall distance d under various solvent viscosity ratios β at $\epsilon De^2 = 1$, L_s=0.1, and κ=10.

Furthermore, to quantitatively characterize the overall influence of the steric factor ν and the solvent viscosity ratio β on the elastic stress field, two integral measures are introduced: the normal stress integral $\Sigma_n = \int_0^1 \tau_{xx}\, dy$ and the shear stress integral $\Sigma_s = \int_0^1 |\tau_{xy}|\, dy$, which represent the total elastic energy storage intensity and the cumulative shear strength over the channel cross-section, respectively. Fig. 8 summarizes the variations of these two quantities with ν and β. As ν increases from 0 to 0.3, Σ_n decreases steadily from 2.74 to 2.01, corresponding to a reduction of approximately 26.8%, whereas Σ_s remains nearly unchanged at about 0.0683, with fluctuations below 0.1%. This pronounced quantitative contrast directly confirms the mechanism inferred from Fig. 6. Specifically, steric hindrance primarily suppresses the tensile elastic response of polymer chains, thereby reducing the overall elastic energy storage. In contrast, the total shear strength within the cross-section is essentially preserved. This observation indicates that the reduction of the near-wall stress peak is largely compensated by the simultaneous expansion of the stress-affected region, providing quantitative evidence for a stress-redistribution mechanism rather than a net loss of shear stress. A fundamentally different trend is observed for the solvent viscosity ratio. As β increases from 0.1 to 0.6, both Σ_n and Σ_s decrease monotonically and almost proportionally, with total reductions of 67.7% and 60.5%, respectively. The synchronous attenuation of the two integrals indicates that increasing β weakens the polymeric elastic contribution throughout the entire channel without inducing any appreciable redistribution of the stress field. Consequently, the effect of β can be interpreted as a nearly uniform

scaling of the elastic stress magnitude, in sharp contrast to the steric factor, which modifies the spatial allocation of elastic stresses while largely preserving the overall shear strength.

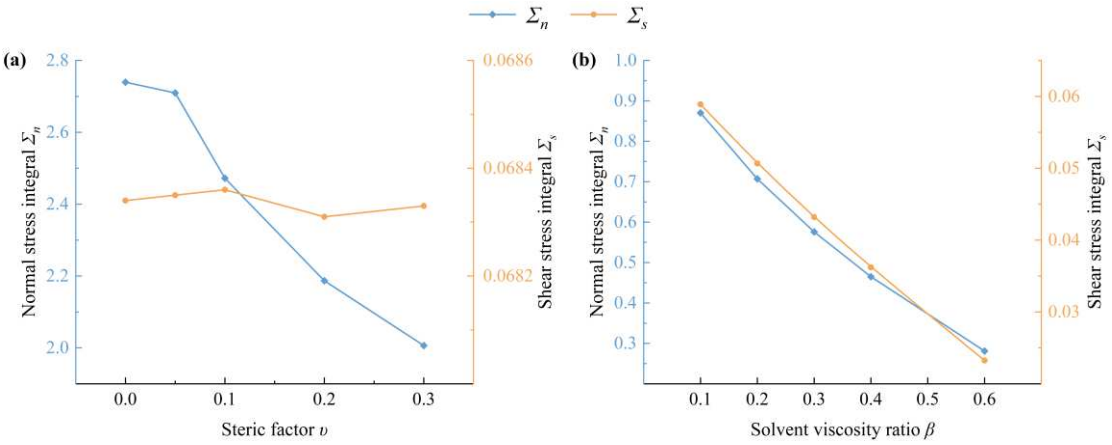


Fig. 8. Variations of Σ_n and Σ_s at $\epsilon De^2 = 1$, L_s=0.1, and κ=20: (a) with the steric factor ν, (b) with the solvent viscosity ratio β.

In summary, ν indirectly reshapes the stress distribution field through charge restructuring, whereas β directly scales the stress magnitude through rheological partitioning; together they constitute two orthogonal elastic stress regulatory dimensions in viscoelastic EOF. The integral quantities Σ_n and Σ_s, as quantitatively comparable global metrics, provide a crucial bridge to the subsequent analysis linking velocity reshaping and thermal transport response.

4.2 Velocity Field Reshaping via Stress Feedback

The preceding section demonstrated that steric hindrance does not simply attenuate the magnitude of elastic stresses; rather, it fundamentally restructures the elastic stress field, as evidenced by peak suppression, broadening of the stress-action zone, and stress crossover. In viscoelastic EOF, such modifications of the stress field alter the effective viscosity through the sPTT constitutive relation. Since the shear stress is fixed by the force balance (Eq. 14), any change in the effective viscosity directly translates into a change in the velocity gradient (Eq. 12), thereby reshaping the velocity field.

Fig. 9 compares the dimensionless velocity profiles of the sPTT fluid in the solvent-free limit (β=0) with those of a Newtonian fluid for different steric factors ν. For both fluids, the velocity decreases monotonically with increasing ν, reflecting the suppression of the net charge density within the EDL by finite ion-size effects. The result-

ing reduction in electroosmotic body force weakens the electrokinetic driving mechanism, producing a common deceleration trend in both fluid systems. Despite this similarity, the sPTT fluid consistently exhibits higher velocities and steeper near-wall velocity gradients than the Newtonian fluid. However, this advantage gradually diminishes as ν increases. At ν=0, the centerline velocity of the sPTT fluid exceeds that of the Newtonian fluid by approximately 53%, whereas at ν=0.3 the two velocity profiles become nearly indistinguishable. This progressive convergence originates from the weakening of the additional transport associated with viscoelastic stresses. In the near-wall high-shear region, polymer chains undergo substantial stretching, generating significant elastic normal stresses. These stresses do not act as an additional driving force—the axial momentum balance (Eq. 13) contains only τ_{xy}. Instead, the normal stress enters the constitutive relation through the stress function $f(\tau_{xx})$, reducing the effective viscosity near the wall. This shear-thinning effect allows the shear stress established by the force balance to generate a larger velocity gradient, thereby increasing the overall flow velocity. As the steric factor increases, two coupled effects emerge. First, the electroosmotic body force is directly weakened owing to the reduction in EDL charge density. Second, the diminished near-wall shear rate suppresses polymer stretching and consequently reduces the generation of elastic normal stresses. As shown in Section 4.1, the peak normal stress decreases by nearly 80% when ν reaches 0.3. The simultaneous attenuation of both the electrokinetic body force and the shear-thinning effect—the latter arising from the quadratic decay of τ_{xx} with τ_{xy}—progressively eliminates the velocity enhancement characteristic of the viscoelastic fluid.

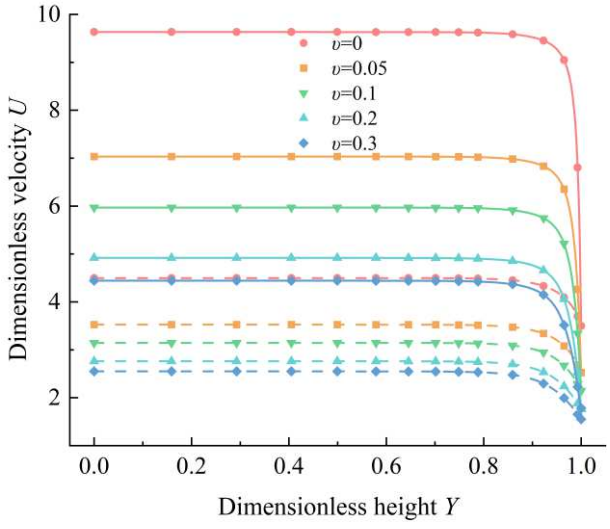


Fig. 9. Longitudinal distribution of the dimensionless velocity U at L_s=0.1, κ=20: solid lines represent the sPTT fluid at $\epsilon De^2 = 1$, dashed lines represent the

Newtonian fluid.

Fig. 10 illustrates the effects of the Debye parameter κ and the slip length L_s on the flow behavior of the sPTT fluid, characterized by the dimensionless average velocity $U_{avg} = \int_0^1 U\, dY$. Fig. 10a shows that U_{avg} increases monotonically with increasing κ, corresponding to the progressive thinning of the EDL and the consequent concentration of net charge near the wall. Interestingly, the suppressive effect of the steric factor ν on the flow velocity becomes increasingly pronounced at high κ. At first glance, this appears counterintuitive, since a thinner EDL would be expected to diminish the influence of steric hindrance. The underlying mechanism, however, is associated with the κ-dependent restructuring of the elastic stress field. At high κ, the EDL occupies only a small fraction of the channel height, resulting in a highly localized shear layer and severely limiting the space available for polymer stretching. When steric hindrance is introduced, ion accumulation is further constrained by volume-exclusion effects, causing an additional contraction of the already narrow shear layer and a substantial reduction in normal-stress generation. Although steric hindrance simultaneously attenuates the stress peak and broadens the stress-action region, the scope for such broadening becomes increasingly limited as the EDL thickness decreases. Consequently, elastic-stress feedback is significantly weakened, making the velocity more sensitive to ν. In contrast, at low κ, the EDL extends farther into the channel and the shear layer occupies a broader region. Although steric hindrance still weakens the electroosmotic body force, the remaining elastic stresses can continue to redistribute momentum over a larger spatial domain, resulting in a comparatively moderate reduction in velocity. These results indicate that the spatial extent of the EDL-controlled shear layer plays an important role in determining the effectiveness of elastic-stress feedback.

Fig. 10b demonstrates the effect of the slip length L_s on the flow velocity and its coupling with the steric factor. The average velocity increases almost linearly with L_s owing to the direct reduction in wall resistance under slip conditions. However, increasing ν reduces the slope of the U_{avg}-L_s relationship. The origin of this behavior lies not in a direct modification of slip itself, but in the suppression of the elastic-stress-feedback pathway by steric hindrance. Under slip conditions, although the wall shear rate is reduced by slip, the normal stress generated in the high-shear EDL region still reduces the effective viscosity through $f(\tau_{xx})$. This shear-thinning contribution constitutes the primary source of the extra velocity gain observed in the sPTT fluid under slip boundary

conditions. As ν increases, the peak normal stress decreases significantly and, despite a slight broadening of the stress-action region, the overall elastic-stress intensity is reduced. Consequently, the elastic enhancement effect weakens, and the synergistic flow promotion associated with slip is substantially diminished.

Therefore, the steric factor does not directly modify the slip boundary condition itself; rather, it indirectly limits the flow-enhancing capability of slip through its restructuring of the elastic stress field. Such stress-redistribution-mediated attenuation of slip effectiveness has no counterpart in the linear momentum response of Newtonian EOF, highlighting the indirect regulatory role of steric hindrance in viscoelastic electroosmotic transport.

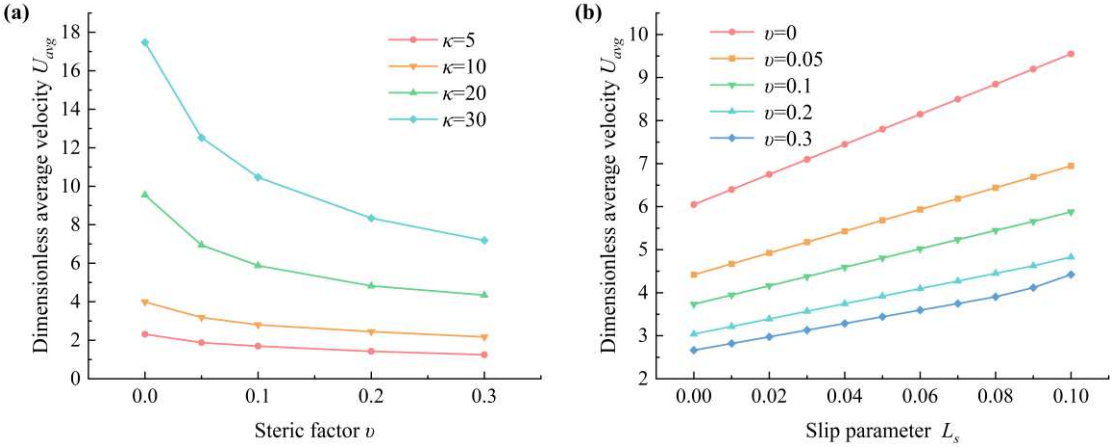


Fig. 10. Variation of the dimensionless average velocity U_{avg} at $\epsilon De^2 = 1$: (a) dimensionless average velocity U_{avg} *vs*. steric factor ν under different Debye parameters κ at L_s=0.1; (b) dimensionless average velocity U_{avg} *vs*. slip parameter L_s under different steric factors ν at κ=20.

Fig. 11a and b illustrate the effects of the solvent viscosity ratio β and the viscoelastic extensibility parameter ϵDe^2 on the flow velocity, further highlighting the multiple pathways through which elastic stresses regulate electroosmotic transport. As shown in Fig. 11a, the dimensionless average velocity U_{avg} decreases monotonically with increasing β, while the velocity curves corresponding to different steric factors ν remain nearly parallel. This indicates that ν and β influence the flow largely independently. Specifically, β weakens the additional momentum transport associated with elastic stresses by reducing the polymeric contribution to the total stress, whereas ν modifies the electroosmotic body force through EDL charge redistribution. These two parameters therefore represent distinct regulatory pathways, namely rheological-property control and body-force control.

Fig. 11b shows that U_{avg} increases with the extensibility parameter ϵDe^2, owing to the enhanced shear-thinning effect and the resulting reduction in near-wall effective viscosity. However, the growth rate gradually decreases as ν increases. This behavior arises because steric hindrance weakens the electroosmotic body force, thereby limiting polymer stretching and reducing the ability of elastic stresses to enhance momentum transport. Consequently, the velocity gain associated with increasing ϵDe^2 becomes progressively smaller, particularly at large ϵDe^2, where the elastic contribution is more pronounced.

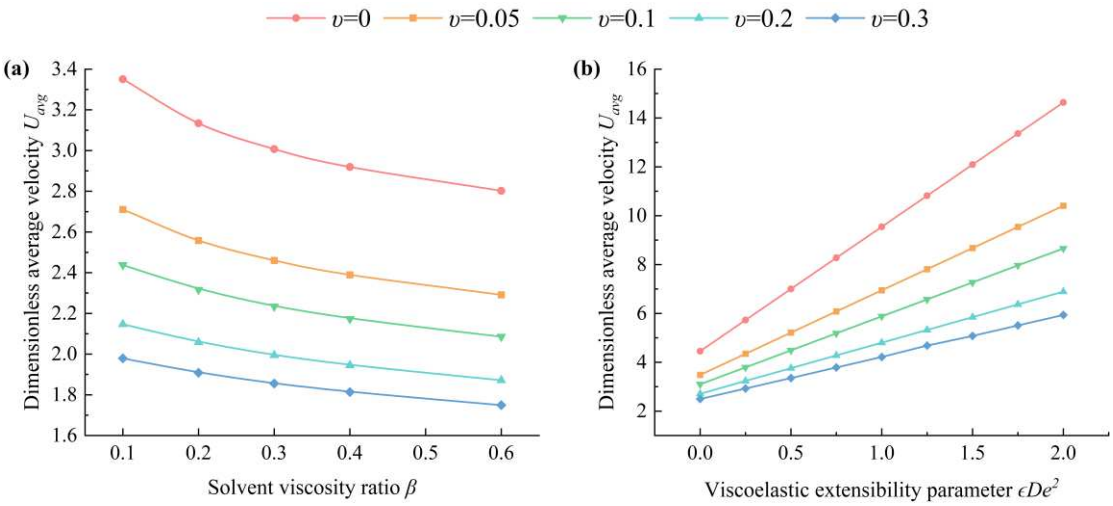


Fig. 11. Variation of the dimensionless average velocity U_{avg} with the solvent viscosity ratio β (a) and the viscoelastic extensibility parameter ϵDe^2 (b) under different steric factors ν at $L_s = 0.1$ and $\kappa = 20$.

4.3 Stress-Mediated Thermal Transport and Temperature Response

Stress restructuring modifies the velocity field through elastic-stress feedback, and the resulting changes in the flow field subsequently affect the energy transport process. The temperature response therefore fundamentally reflects the coupling between momentum and thermal transport. In viscoelastic EOF, the temperature distribution is governed not only by convective heat transfer but also by internal heat-generation mechanisms such as viscous dissipation. Since these thermal effects are closely linked to the flow state, the stress–velocity coupling discussed above is ultimately manifested in the evolution of the temperature field.

This section examines the influence of steric hindrance on the temperature field and the underlying physical mechanism. Fig. 12 compares the dimensionless temperature θ as a function of ν for a Newtonian fluid and an sPTT fluid in the solvent-free limit under a constant wall heat flux of q=15000 W/m^2 and Pe=0.05. For both fluids, θ

increases monotonically with increasing ν, reflecting the inevitable deterioration of convective heat-transfer capability caused by the attenuation of the electroosmotic driving force. At the same ν, however, the temperature of the sPTT fluid remains consistently lower than that of the Newtonian fluid, and the difference becomes more pronounced as ν decreases and elastic effects become stronger. This behavior can be attributed to the shear-thinning-induced near-wall velocity enhancement arising from elastic normal stresses. Under the same driving force, the sPTT fluid maintains a higher effective thermal capacity rate, allowing heat to be transported downstream more efficiently and reducing thermal accumulation within the cross-section. In contrast, the Newtonian fluid responds only through the direct velocity reduction caused by steric hindrance and lacks this elastic enhancement mechanism for convective heat transfer.

Furthermore, the nearly uniform temperature distribution across the channel cross-section, with variations below 1%, confirms the dominant role of transverse thermal diffusion in temperature homogenization at such a low *Pe*. Nevertheless, the overall fluid temperature rise remains governed by the efficiency of axial convective transport, such that differences in flow velocity are directly reflected in the corresponding temperature response.

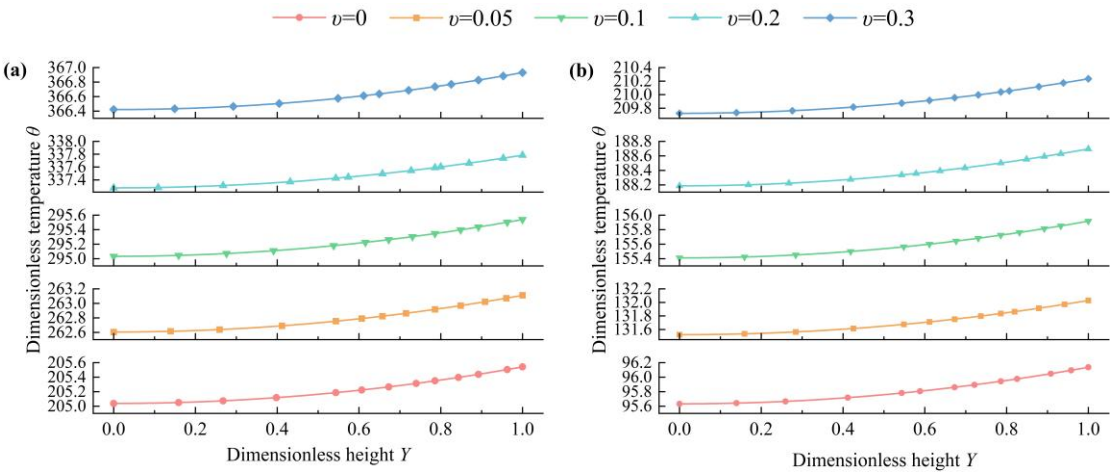


Fig. 12. Variation of the dimensionless temperature θ at X=0.5 for q=15000 W/m^2, Pe=0.05, L_s=0.1 and κ=20: (a) Newtonian fluid, (b) sPTT fluid at $\epsilon De^2 = 1$.

Fig. 13a further illustrates the coupled effects of the Debye parameter κ and the steric factor ν on the cross-sectional mean temperature θ_m. Overall, θ_m decreases with increasing κ, owing to the enhancement of electroosmotic convection associated with a thinner EDL. However, the temperature increase induced by ν is markedly amplified

in the low-κ (thick EDL) regime, which is opposite to the enhanced velocity sensitivity to ν observed in the high-κ regime in Section 4.2. This discrepancy arises primarily from the greater vulnerability of thermal transport to the loss of elastic-stress feedback under weak-convection conditions. At low κ, the baseline velocity is relatively small and the convective heat-removal capacity is limited; consequently, the shear-thinning effect induced by elastic normal stresses becomes crucial for sustaining near-wall convective transport. When steric hindrance is introduced, it not only weakens the Coulomb body force directly but also significantly suppresses this additional momentum-transfer mechanism through the attenuation of normal stresses. As discussed in Section 4.1, the peak normal stress decreases by nearly 80% at ν=0.3. In a thick EDL, such attenuation further weakens the already limited convective transport capability, so that even a modest reduction in velocity can lead to a pronounced increase in heat accumulation. By contrast, at high κ, the stronger flow and enhanced convection render the thermal boundary layer less dependent on elastic-stress feedback, resulting in a comparatively weak temperature response to steric effects.

Fig. 13b presents the influence of the slip length L_s on θ_m. The monotonic decrease of θ_m with increasing L_s reflects a dual cooling mechanism unique to the sPTT fluid. On the one hand, slip enhances convective heat transfer by increasing the flow velocity; on the other hand, it directly reduces elastic dissipation heating by lowering the shear and extensional rates throughout the channel. The latter mechanism is characteristic of viscoelastic fluids and is absent in Newtonian systems. Increasing ν elevates the overall temperature level because both the electroosmotic driving force and the convective transport capacity are reduced. Nevertheless, the slopes of the θ_m-L_s curves remain nearly identical for different values of ν, with only a noticeable temperature offset between ν=0.3 and the point-charge limit ν=0. This observation indicates that steric hindrance primarily shifts the temperature baseline through its influence on flow velocity, while exerting little effect on the dependence of elastic dissipation on slip. Although ν restructures the stress distribution, the total cross-sectional shear strength Σ_s remains nearly unchanged, and the dissipation heating therefore continues to be governed predominantly by Σ_s.

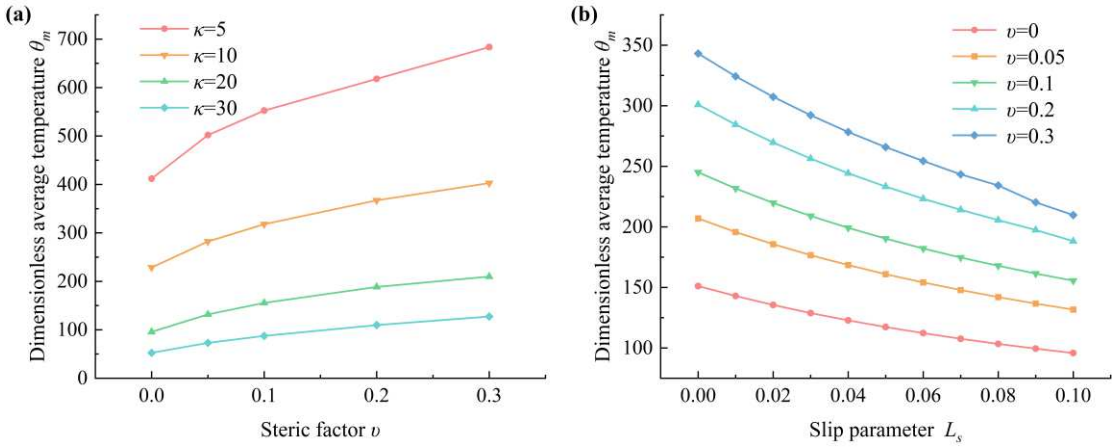


Fig. 13. Variation of the dimensionless mean temperature θ_m at X=0.5 for q=15000 W/m^2, Pe=0.05 and $\epsilon De^2 = 1$: (a) with the steric factor ν under different Debye parameters at L_s=0.1; (b) with the slip length L_s under different steric factors at κ=20.

Fig. 14a and b illustrate the effects of the solvent viscosity ratio β and the viscoelastic extensibility parameter ϵDe^2 on the cross-sectional mean temperature θ_m, respectively. In Fig. 14a, θ_m increases monotonically with increasing β, and the corresponding increments for different values of ν remain nearly parallel. The increase in β raises the temperature through two concurrent mechanisms. First, it reduces the flow velocity and consequently weakens convective heat transfer. Second, the enhanced solvent viscous contribution increases near-wall viscous dissipation heating. The steric factor ν primarily shifts the overall temperature level without significantly altering the slope of the increase, which is fully consistent with the independent influences of ν and β on the velocity field. Specifically, β governs the partitioning between elastic and viscous contributions, whereas ν controls the magnitude of the electroosmotic body force; thus, the two parameters operate through distinct and largely orthogonal regulatory pathways.

In Fig. 14b, θ_m decreases with increasing ϵDe^2 owing to the reduction in effective viscosity and the enhancement of convective transport associated with stronger elastic stretching. Notably, the slopes of the θ_m-ϵDe^2 curves exhibit only minor differences among various values of ν, in sharp contrast to the pronounced suppression of the ϵDe^2-induced velocity enhancement by steric hindrance observed in the velocity field. This velocity–temperature sensitivity mismatch can be interpreted as a nonlinear thermal compensation effect. At high ν, the baseline velocity is relatively low and the temperature rise is substantial, so the marginal efficiency of convective cooling is high, and a given increase in velocity produces a larger temperature reduction. At low ν, the

velocity is already high and the temperature approaches its lower limit; consequently, the cooling response enters a regime of diminishing returns, where even a larger velocity increase yields only a modest temperature decrease. These opposing effects largely offset each other, leading to a convergence of the temperature-response slopes with respect to ϵDe^2 for different values of ν.

Consequently, ϵDe^2 constitutes an independent temperature-regulation parameter that is relatively insensitive to ion-size effects, complementing the role of ν, which indirectly constrains velocity enhancement through stress redistribution. Whereas ϵDe^2 regulates convective transport efficiency without altering the stress-field structure, ν simultaneously influences convection and dissipation through its restructuring of the elastic stress field.

In summary, the temperature field in sPTT viscoelastic EOF is not determined solely by the flow velocity, but is governed by a complete causal chain of stress redistribution → velocity restructuring → competition between convection and dissipation. In the thick-EDL regime, where convective transport is inherently weak, the loss of elastic-stress feedback is nonlinearly amplified. Meanwhile, the slip and elastic parameters provide independent temperature-regulation windows through distinct physical pathways.

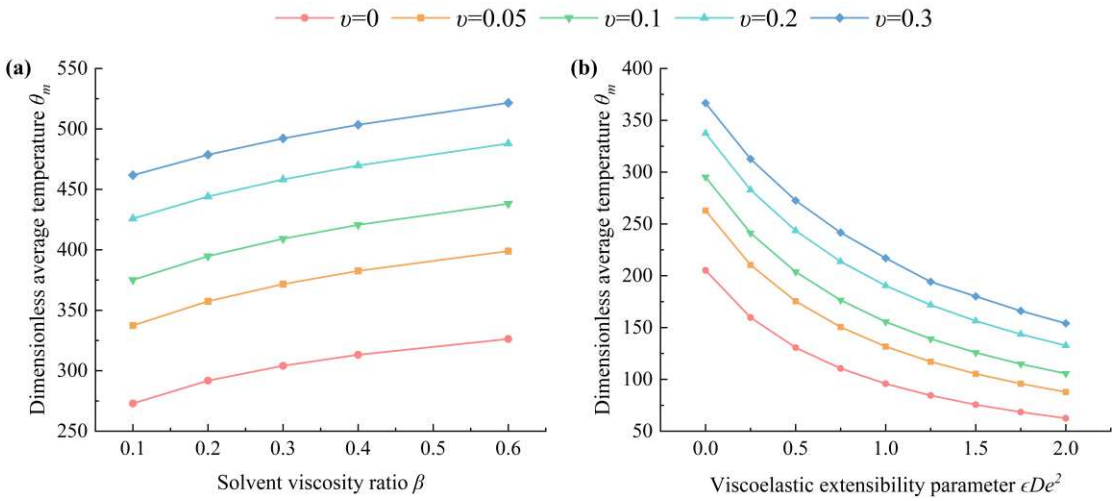


Fig. 14. Variation of the dimensionless mean temperature θ_m at X=0.5 under different steric factors ν for q=15000 W/m^2, Pe=0.05, L_s = 0.1 and κ=20: (a) with the solvent viscosity ratio β, (b) with the viscoelastic extensibility parameter ϵDe^2.

4.4 Thermal Transport Regulation Mechanisms

The preceding analysis has shown that steric-induced stress redistribution can modify the temperature field through velocity-feedback effects, thereby establishing a

complete stress–flow–heat transfer response chain. As a key indicator of overall thermal transport performance, the Nusselt number *Nu* reflects the net outcome of the competition between convective heat transfer and dissipation-induced heating. Accordingly, this section investigates the effects of parameters such as *Br*, κ, and L_s on *Nu*, with the aim of elucidating the dominant mechanisms responsible for heat transfer enhancement or suppression under different conditions.

Fig. 15 presents the influence of the steric factor ν on the local Nusselt number along the channel length *X* for the sPTT fluid at *Br*=0.025 and *Pe*=0.1. Under these conditions, *Nu* increases slightly with increasing ν, exhibiting a trend distinct from that observed in the purely convection-dominated regime. As ν increases, ion accumulation within the EDL is restricted by finite ion-size effects, while the near-wall velocity gradient is simultaneously reduced, leading to a corresponding attenuation of viscous dissipation heating. The weakening of the internal heat source decreases the wall-to-fluid temperature difference, and the relatively larger reduction in this temperature difference results in an increase in *Nu*.

Notably, the elastic normal stresses in the sPTT fluid sustain a certain level of near-wall momentum transport (see Sections 4.1–4.2), thereby mitigating the adverse effect of the reduced mean flow velocity on convective heat transfer. This elastic sustaining effect prevents *Nu* from decreasing as ν increases and instead allows a slight enhancement under the dominant influence of dissipation suppression. Such a response is absent in Newtonian fluids.

Furthermore, the nearly constant *Nu* along the streamwise direction indicates that, under the low-convection condition of *Pe*=0.1, the thermal boundary layer reaches a fully developed state within a short distance from the inlet. The steric factor therefore modifies only the overall magnitude of *Nu* without introducing any significant streamwise dependence. Based on this observation, the cross-section at *X*=0.5 is adopted in the following analysis as a representative location for characterizing the overall heat transfer performance of the microchannel.

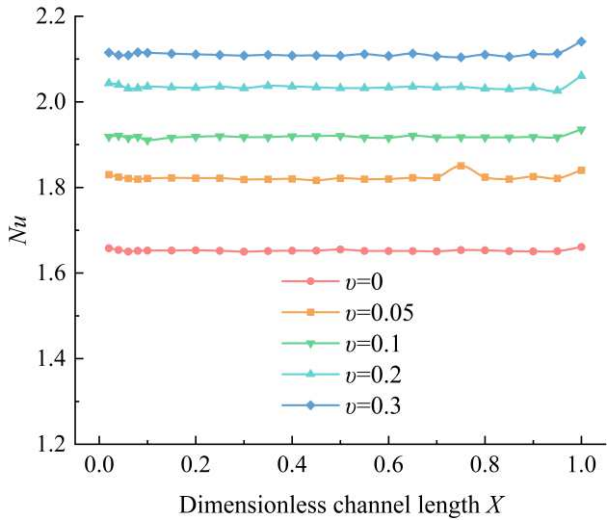


Fig. 15. Variation of *Nu* along the channel length *X* with the steric factor ν at *Br*=0.025, *Pe*=0.1, L_s=0.1 and κ=20.

Fig. 16 compares the influence of the steric factor ν on *Nu* as a function of *Br* for a Newtonian fluid (Fig. 16a) and an sPTT fluid with β=0.2 (Fig. 16b). For both fluids, *Nu* decreases monotonically with increasing *Br*, reflecting the inevitable enhancement of viscous dissipation heating, which raises the mean fluid temperature and weakens the wall-to-fluid temperature gradient. However, the effect of ν on *Nu* reverses upon crossing a critical Brinkman number, Br_c. A reversal of the steric effect on Nu across a critical Brinkman number has recently been reported for pure EOF of Newtonian fluids with interfacial slip [30]. The present results show that in sPTT fluids this reversal threshold shifts to a significantly lower Brinkman number and the sensitivity to ion size is markedly amplified, which we attribute to a viscous–elastic dual-channel dissipation-suppression mechanism that has no counterpart in Newtonian systemsIn the low-*Br* regime, where convection dominates thermal transport, steric hindrance weakens the electroosmotic body force and suppresses convection, resulting in a decrease in *Nu*. In contrast, in the high-*Br* regime, where dissipation plays a dominant role in determining the temperature field, steric hindrance reduces dissipation heating by lowering the near-wall shear rate, leading to an increase in *Nu*.

Although this reversal behavior is observed in both fluids, the critical Brinkman number of the sPTT fluid is significantly lower, and the separation among the *Nu* curves corresponding to different values of ν becomes much more pronounced in the high-*Br* regime. This difference arises because the viscoelastic fluid possesses additional dissipation-suppression mechanisms that are absent in the Newtonian fluid. At β=0.2,

increasing ν induces a redistribution of the elastic stress field, characterized by attenuation of the normal-stress peak and broadening of the shear layer. This restructuring not only directly reduces polymeric elastic dissipation, but also suppresses solvent viscous dissipation through the reduction of the near-wall shear rate. As a result, a viscous–elastic dual-channel dissipation-suppression mechanism is established.

The combined action of these two pathways enables the dissipation heat source to be controlled more effectively and at a lower *Br*. Consequently, the reversal threshold occurs earlier in the sPTT fluid, and its thermal response to steric effects becomes significantly more sensitive in the dissipation-dominated regime.

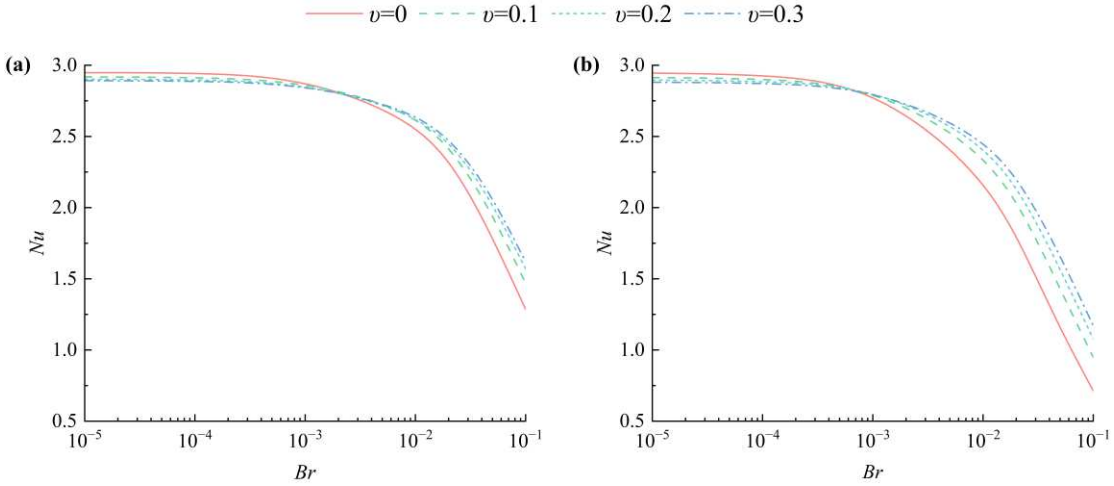


Fig. 16. Variation of *Nu* with *Br* at *X*=0.5 under different steric factors ν for *Pe*=0.1, L_s=0.1 and κ=20: (a) Newtonian fluid, (b) sPTT fluid at $\epsilon De^2 = 1$ and β=0.2.

Fig. 17 illustrates the dependence of *Nu* on the Debye parameter κ and the slip length L_s. Fig. 17a presents the coupled effects of κ and the steric factor ν on *Nu*. Overall, *Nu* increases with increasing κ owing to the enhancement of electroosmotic convection associated with a thinner EDL. However, the suppressive effect of ν on *Nu* becomes markedly stronger in the thick-EDL (low-κ) regime. At κ=5, increasing ν from 0 to 0.3 reduces *Nu* from 2.75 to 2.50, corresponding to a decrease of approximately 9%, whereas at κ=30 the reduction is only from 2.97 to 2.92. This behavior contrasts with the velocity sensitivity to ν discussed in Section 4.2.

The origin of this sensitivity mismatch lies in the nonlinear amplification of elastic-stress-feedback loss under weak-convection conditions. At low κ, the baseline velocity is relatively low and the convective heat-removal capacity is limited. Under such conditions, the additional momentum transport generated by elastic normal stresses

plays a crucial role in sustaining near-wall thermal boundary-layer renewal. When steric hindrance is introduced, it not only weakens the Coulomb body force directly but also suppresses this additional transport pathway through the attenuation of normal stresses, further reducing convective heat-transfer efficiency. As a result, even a modest reduction in velocity can lead to a substantial increase in heat accumulation, causing a pronounced decrease in *Nu*. In contrast, at high κ, the stronger flow and enhanced convection buffer the loss of elastic-stress feedback, rendering *Nu* comparatively insensitive to ν. These results indicate that the sensitivity of *Nu* is governed not by the magnitude of κ itself, but by the relative contribution of elastic-stress feedback to the overall convective heat-transfer process. This contribution becomes increasingly important at low κ, giving rise to a thermally sensitive response window.

Fig. 17b shows the influence of the slip length L_s on *Nu*. The Nusselt number increases monotonically with increasing L_s. Slip enhances convective heat transfer by reducing flow resistance, while simultaneously suppressing elastic dissipation heating through the reduction of the shear rate throughout the channel. The latter mechanism is unique to viscoelastic fluids. Increasing ν lowers the overall level of *Nu* because both the electroosmotic driving force and the convective transport capacity decrease. At the same time, however, the slope of the *Nu*-L_s curve becomes steeper. This behavior arises because, after steric hindrance reduces the baseline velocity, the relative contribution of slip-induced velocity enhancement becomes more significant. Moreover, the suppression of normal stresses at high ν makes the drag-reducing effect of slip on the near-wall shear layer more pronounced. Together, these effects partially compensate for the convective loss caused by steric hindrance.

This slip-induced compensation complements the stress-redistribution-mediated attenuation of slip effectiveness discussed earlier. Although steric hindrance weakens the absolute strength of the slip–elasticity synergistic enhancement mechanism, it simultaneously increases the relative regulatory influence of the slip pathway within the remaining convective transport process.

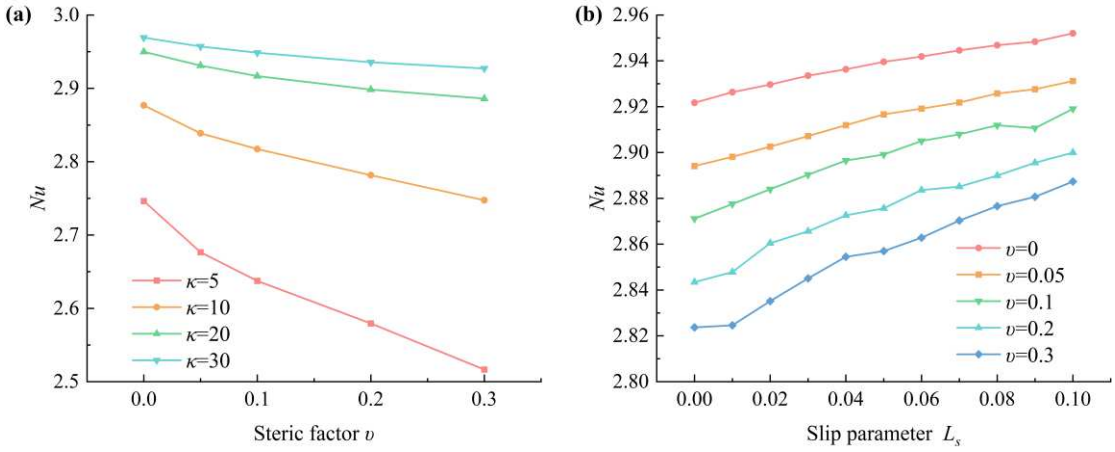


Fig. 17. Variation of *Nu* for the sPTT fluid at $\epsilon De^2 = 1$: (a) with the steric factor ν under different Debye parameters κ at L_s=0.1; (b) with the slip parameter L_s under different steric factors ν at κ=20.

Overall, the results establish an electro–elastic–thermal coupling framework for viscoelastic EOF, revealing how microscopic ionic redistribution can propagate through elastic stress feedback to regulate macroscopic heat transfer. Specifically, the steric effect modifies the ion distribution within the electric double layer (EDL), thereby weakening the electroosmotic driving force while simultaneously redistributing the polymeric elastic stresses. This stress redistribution further modifies the effective viscosity and reshapes the velocity field, consequently influencing convective heat transfer and the spatial distribution of viscous and elastic dissipation. The resulting competition between convection and dissipation governs the thermal boundary-layer response and gives rise to distinct Nusselt number behaviors under different operating conditions. In addition, interfacial slip provides an important means of regulating this coupled process by enhancing convective transport while suppressing elastic dissipation. These findings clarify the fundamental differences between heat transfer in viscoelastic and Newtonian EOF and provide a unified theoretical basis for understanding the combined effects of ion-size constraints, wall slip, and fluid elasticity on microchannel heat transfer.

5.Conclusions

This study systematically investigated the flow and heat transfer characteristics of EOF in a microchannel under the coupled effects of steric hindrance, interfacial slip, and elastic stresses using the sPTT viscoelastic fluid model. The main conclusions are summarized as follows.

(1) Core finding: steric-hindrance-induced stress restructuring. Unlike Newtonian fluids, in which steric effects merely weaken the electroosmotic body force through modifications of the EDL charge distribution, steric hindrance in sPTT fluids additionally induces a restructuring of the elastic stress field. Specifically, the near-wall peaks of both the normal and shear stresses decrease significantly, while their regions of influence broaden toward the channel interior, leading to stress-profile crossover near the outer edge of the EDL. Integral analysis further demonstrates that steric hindrance primarily redistributes the elastic stress field rather than uniformly reducing its overall strength. By contrast, the solvent viscosity ratio produces an approximately uniform attenuation of the stress magnitude. These two parameters therefore constitute two orthogonal dimensions of elastic-stress regulation.

(2) Operating mechanism: stress restructuring reshapes the velocity field through elastic feedback. The elastic normal stress reduces the near-wall effective viscosity through the constitutive stress function (shear thinning), allowing the fixed electroosmotic shear stress to generate a larger velocity gradient. At low steric factors, this mechanism is strong and promotes a more pronounced plug-like velocity profile. As the steric factor increases, the elastic feedback weakens and the velocity advantage of the sPTT fluid progressively diminishes. Furthermore, the flow-enhancing effect of wall slip is indirectly reduced through steric suppression of the normal stress, giving rise to a stress-restructuring-mediated attenuation of slip effectiveness that has no counterpart in Newtonian fluids.

(3) Macroscopic manifestation: competition between convection and dissipation governs the multi-mode response of *Nu*. The temperature field and Nusselt number are not direct linear reflections of the velocity field, but are determined by the competition between convective heat transfer and dissipation-induced heating. In the low-*Br* regime, convection dominates thermal transport and steric hindrance deteriorates heat transfer. In the high-*Br* regime, dissipation becomes dominant, and steric hindrance enhances heat transfer by simultaneously suppressing viscous and elastic dissipation, leading to a reversal in the response of *Nu* near a critical Brinkman number. The reversal threshold for the sPTT fluid is significantly lower than that of the Newtonian fluid. In the thick-EDL regime, where baseline convection is relatively weak, heat accumulation is strongly amplified after steric hindrance weakens elastic-stress feedback. In contrast, in the thin-EDL regime, the stronger convective transport effectively compensates for the loss of elastic feedback. Meanwhile, wall slip serves as a dual-channel heat-transfer

enhancement mechanism by simultaneously strengthening convection and reducing elastic dissipation.

(4) Unified electro–elastic–thermal coupling mechanism. This study establishes a cross-scale coupling pathway linking steric-induced EDL restructuring to elastic stress redistribution, velocity-field reshaping, and the resulting competition between convective heat transfer and dissipation-induced heating. The interplay of these processes governs the thermal response and Nusselt number of viscoelastic EOF. Meanwhile, interfacial slip provides an additional means of regulating heat transfer by enhancing convection and suppressing elastic dissipation.

More importantly, this study reveals a broader class of cross-scale coupling mechanisms. Variations in microscopic ion distributions are not confined to local electrostatic responses; instead, they are transmitted through viscoelastic stress feedback to the momentum and thermal transport processes, ultimately producing substantial changes in macroscopic heat-transfer performance. The electro–elastic–thermal framework developed herein is not tied to a particular set of model parameters. Its underlying physical principles can be extended to electrokinetic transport and thermal-management problems involving polyelectrolyte solutions, biological fluids, and other complex fluids, thereby providing a unified physical perspective for the design and optimization of multi-physics microfluidic systems.

CRediT authorship contribution statement

Kuanhong Peng: Conceptualization (equal); Data curation (equal); Formal analysis (equal); Investigation (equal); Methodology (equal); Software (equal); Validation (equal); Visualization (equal); Writing–original draft (equal). **Weicheng Yu**: Conceptualization (equal); Data curation (equal); Formal analysis (equal); Investigation (equal); **Yifei Sun**: Methodology (equal); Software (equal); Validation (equal); Visualization (equal). **Jie Li**: Methodology (equal); Resources (equal); Supervision (equal); Visualization (equal); Writing–review & editing (equal).

Data availability

The data that support the findings of this study are available from the corresponding author upon reasonable request.

Declaration of competing interest

The authors declare that they have no known competing financial interests or personal relationships that could have appeared to influence the work reported in this paper.

Funding Declaration

This research received no external funding.

References

[1] A. Raj, A.K. Sen, Entry and passage behavior of biological cells in a constricted compliant microchannel, RSC Adv. 8 (2018) 20884–20893. https://doi.org/10.1039/C8RA02763C

[2] P.K. Wong, T.H. Wang, J.H. Deval, C.M. Ho, Electrokinetics in micro devices for biotechnology applications, IEEE/ASME Trans. Mechatron. 9 (2004) 366–376. https://doi.org/10.1109/TMECH.2004.828659

[3] K. Horiuchi, P. Dutta, Joule heating effects in electroosmotically driven microchannel flows, Int. J. Heat Mass Transf. 47 (2004) 3085–3095. https://doi.org/10.1016/j.ijheatmasstransfer.2004.02.020

[4] Sanjay, A.R. Harikrishnan, Interplay of high zeta potential and steric factor on the slip thermofluidics of power-law fluids through narrow confinements, Int. J. Heat Mass Transf. 185 (2022) 122426. https://doi.org/10.1016/j.ijheatmasstransfer.2021.122426

[5] M. Yang, M.T. Li, Y.C. Hua, W. Wang, B.Y. Cao, Experimental study on single-phase hybrid microchannel cooling using HFE-7100 for liquid-cooled chips, Int. J. Heat Mass Transf. 160 (2020) 120230. https://doi.org/10.1016/j.ijheatmasstransfer.2020.120230

[6] N. Gilmore, V. Timchenko, C. Menictas, Open manifold microchannel heat sink for high heat flux electronic cooling with a reduced pressure drop, Int. J. Heat Mass Transf. 163 (2020) 120395. https://doi.org/10.1016/j.ijheatmasstransfer.2020.120395

[7] H. Shen, G. Xie, C.C. Wang, H. Liu, Experimental and numerical examinations of thermofluids characteristics of double-layer microchannel heat sinks with deflectors, Int. J. Heat Mass Transf. 182 (2022) 121961. https://doi.org/10.1016/j.ijheatmasstransfer.2021.121961

[8] H. Tan, L. Wu, M. Wang, Z. Yang, P. Du, Heat transfer improvement in microchannel heat sink by topology design and optimization for high heat flux chip cooling, Int. J. Heat Mass Transf. 129 (2019) 681–689. https://doi.org/10.1016/j.ijheatmasstransfer.2018.09.092

[9] S. Pabi, S.K. Mehta, S. Pati, Analysis of thermal transport and entropy generation characteristics for electroosmotic flow through a hydrophobic microchannel considering viscoelectric effect, Int. Commun. Heat Mass Transf. 127 (2021) 105519. https://doi.org/10.1016/j.icheatmasstransfer.2021.105519

[10] R. Sarma, N. Deka, K. Sarma, P.K. Mondal, Electroosmotic flow of Phan–Thien–Tanner fluids at high zeta potentials: An exact analytical solution, Phys. Fluids 30 (2018) 062001. https://doi.org/10.1063/1.5033974

[11] K.N. Vasista, S. Mehta, S. Pati, Numerical assessment of hydrodynamic and mixing characteristics for mixed electroosmotic and pressure-driven flow through a wavy microchannel with patchwise surface heterogeneity, Proc. Inst. Mech. Eng. Part E J. Process Mech. Eng. (2021). https://doi.org/10.1177/09544089211051640

[12] P.F. Eng, P. Nithiarasu, A.K. Arnold, P. Igic, O.J. Guy, Electro-osmotic flow based cooling system for microprocessors, in: Proc. EuroSimE 2007, IEEE, London, UK, 2007, pp. 1–5. https://doi.org/10.1109/ESIME.2007.360041

[13] G.Y. Tang, C. Yang, J.C. Chai, H.Q. Gong, Joule heating effect on electroosmotic flow and mass species transport in a microcapillary, Int. J. Heat Mass Transf. 47 (2004) 215–227. https://doi.org/10.1016/j.ijheatmasstransfer.2003.07.006

[14] G.C. Shit, A. Mondal, A. Sinha, P.K. Kundu, Electro-osmotically driven MHD flow and heat transfer in micro-channel, Physica A 449 (2016) 437–454. https://doi.org/10.1016/j.physa.2016.01.008

[15] Y.P. Cheng, C.J. Teo, B.C. Khoo, Microchannel flows with superhydrophobic surfaces: Effects of Reynolds number and pattern width to channel height ratio, Phys. Fluids 21 (2009) 122004. https://doi.org/10.1063/1.3281130

[16] H.S. Gaikwad, D.N. Basu, P.K. Mondal, Slip driven micro-pumping of binary system with a layer of non-conducting fluid under electrical double layer phenomenon, Colloids Surf. A Physicochem. Eng. Asp. 518 (2017) 166–172. https://doi.org/10.1016/j.colsurfa.2017.01.024

[17] D. Jing, Y. Pan, X. Wang, Joule heating, viscous dissipation and convective heat transfer of pressure-driven flow in a microchannel with surface charge-dependent slip, Int. J. Heat Mass Transf. 108 (2017) 1305–1313. https://doi.org/10.1016/j.ijheatmasstransfer.2016.12.090

[18] D. Jing, Y. Pan, Electroviscous effect and convective heat transfer of pressure-driven flow through microtubes with surface charge-dependent slip, Int. J. Heat Mass Transf. 101 (2016) 648–655. https://doi.org/10.1016/j.ijheatmasstransfer.2016.05.087

[19] A.A. Yazdi, A. Sadeghi, M.H. Saidi, Steric effects on electrokinetic flow of

non-linear biofluids, Colloids Surf. A Physicochem. Eng. Asp. 484 (2015) 394–401. https://doi.org/10.1016/j.colsurfa.2015.08.018

[20] Y. Liu, Y. Jian, The effects of finite ionic sizes and wall slip on entropy generation in electroosmotic flows in a soft nanochannel, J. Heat Transfer 141 (2019) 102401. https://doi.org/10.1115/1.4044414

[21] E. Jimenez, J. Escandón, F. Méndez, O. Bautista, Combined viscoelectric and steric effects on the electroosmotic flow in nano/microchannels with heterogeneous zeta potentials, Colloids Surf. A Physicochem. Eng. Asp. 577 (2019) 347–359. https://doi.org/10.1016/j.colsurfa.2019.05.050

[22] A. Bandopadhyay, S. Chakraborty, Ionic size dependent electroosmosis in ion-selective microchannels and nanochannels, Electrophoresis 34 (2013) 2193–2198. https://doi.org/10.1002/elps.201300094

[23] M.Z. Bazant, M.S. Kilic, B.D. Storey, A. Ajdari, Towards an understanding of induced-charge electrokinetics at large applied voltages in concentrated solutions, Adv. Colloid Interface Sci. 152 (2009) 48–88. https://doi.org/10.1016/j.cis.2009.10.001

[24] R. Dey, T. Ghonge, S. Chakraborty, Steric-effect-induced alteration of thermal transport phenomenon for mixed electroosmotic and pressure-driven flows through narrow confinements, Int. J. Heat Mass Transf. 56 (2013) 251–262. https://doi.org/10.1016/j.ijheatmasstransfer.2012.09.038

[25] E. Jimenez, J.P. Escandón, F. Méndez, O. Bautista, Combined viscoelectric and steric effects on the electroosmotic flow in a microchannel under induced high zeta potentials, Colloids Surf. A Physicochem. Eng. Asp. 531 (2017) 221–233. https://doi.org/10.1016/j.colsurfa.2017.04.081

[26] S. Mehta, S. Pati, L. Baranyi, Steric effect induced heat transfer for electroosmotic flow of Carreau fluid through a wavy microchannel, Tech. Mech. 43 (2023) 2–12. https://doi.org/10.24352/UB.OVGU-2023-040

[27] E.M. Jimenez, C.G. Hernández, D.A. Torres, N. Ratkovich, J.P. Escandón, J.R. Gómez, R.O. Vargas, Viscoelectric and steric effects on electroosmotic flow in a soft channel, Mathematics 13 (2025) 2546. https://doi.org/10.3390/math13162546

[28] I. Borukhov, D. Andelman, H. Orland, Steric effects in electrolytes: A modified Poisson–Boltzmann equation, Phys. Rev. Lett. 79 (1997) 435–438. https://doi.org/10.1103/PhysRevLett.79.435

[29] S. Mukherjee, P. Goswami, J. Dhar, S. Dasgupta, S. Chakraborty, Ion-size dependent electroosmosis of viscoelastic fluids in microfluidic channels with interfacial slip, Phys. Fluids 29 (2017) 072002. https://doi.org/10.1063/1.4990841

[30] T. Sujith, S.K. Mehta, S. Pati, Ion size-dependent heat transfer characteristics of electroosmotic flow through a microchannel considering interfacial slip, Phys. Fluids 37 (2025) 032019. https://doi.org/10.1063/5.0257243

[31] Z. Wu, Y. Liu, G. Liu, Electroosmotic flow in graphene nanochannels considering steric effects, Phys. Fluids 36 (2024) 052007. https://doi.org/10.1063/5.0209897

[32] Y. Zhang, G. Zhao, J. Zhang, B. Xue, H. Wang, Y. Jian, Steric effect on the electroosmosis and electrokinetic energy conversion of Jeffrey's nanofluid with couple stress in porous microchannels, J. Mol. Liq. 437 (2025) 128263. https://doi.org/10.1016/j.molliq.2025.128263

[33] T. Sujith, S.K. Mehta, S. Pati, Steric effect induced heat transfer characteristics of electromagnetohydrodynamic electroosmotic flow through a microchannel considering interfacial slip, Phys. Fluids 37 (2025) 052009. https://doi.org/10.1063/5.0267237

[34] M. Kiyasatfar, Convective heat transfer and entropy generation analysis of non-Newtonian power-law fluid flows in parallel-plate and circular microchannels under slip boundary conditions, Int. J. Therm. Sci. 128 (2018) 15–27. https://doi.org/10.1016/j.ijthermalsci.2018.02.013

[35] A. Haque, A.K. Nayak, Mixed electroosmotic pressure driven flow and heat transfer of power-law fluid in a hydrophobic microchannel, in: Proc. ASME FEDSM 2017, FEDSM2017-69525, 2017. https://doi.org/10.1115/FEDSM2017-69525

[36] Sanjay, A.R. Harikrishnan, Slip hydrodynamics of combined electroosm otic and pressure driven flows of power law fluids through narrow confi nements, Eur. J. Mech. – B/Fluids 89 (2021) 525–550. https://doi.org/10.1016/j.euromechflu.2021.07.009

[37] P. Fadaei, H. Niazmand, M.A. Raoufi, Influence of finite size of ions on thermal transport of a simultaneous electrokinetic-pressure driven flow of power-law fluids in a slit microchannel, Colloids Surf. A Physicochem. Eng. Asp. 634 (2022) 127857. https://doi.org/10.1016/j.colsurfa.2021.127857

[38] Y. Liu, J. Xing, Y. Jian, Heat transfer and entropy generation analysis of electroosmotic flows in curved rectangular nanochannels considering the influence of steric effects, Int. Commun. Heat Mass Transf. 139 (2022) 106501. https://doi.org/10.1016/j.icheatmasstransfer.2022.106501

[39] S. Akhtar, N.S. Akbar, J. Akram, M.F. Hussain, T. Muhammad, Heat transfer analysis on blood flow dynamics of hybrid nanoparticles in an asymmetric domain under electroosmotic and microbial effects: A Johnson-Segalman model approach, *Int. J. Heat Fluid Flow* 115 (2025) 109879. https://doi.org/10.1016/j.ijheatfluidflow.2025.109879

[40] T. Kumbalpuri, S. Sarkar, Thermally developing streaming potential-mediated pressure-driven flow of Phan–Thien–Tanner fluid in a microchannel, Phys. Fluids 36 (2024) 072019. https://doi.org/10.1063/5.0220116

[41] T. Kumbalpuri, S. Sarkar, Thermally developing combined electroosmotic and pressure-driven flow of Phan–Thien–Tanner fluids in a microchannel, Phys. Fluids 35 (2023) 082015. https://doi.org/10.1063/5.0166296

[42] M. Kananipour, M.M. Mohseni, R. Jahanmardi, H.A. Khonakdar, Heat and mass transfer analysis of s-PTT nanofluid in microchannels under combined electroosmotic and pressure-driven flows with wall slip using the homotopy perturbation method, Heliyon 10 (2024) e39526. https://doi.org/10.1016/j.heliyon.2024.e39526

[43] S. Sarkar, Streaming-potential-mediated pressure-driven transport of Phan–Thien–Tanner fluids in a microchannel, Phys. Rev. E 101 (2020) 053104. https://doi.org/10.1103/PhysRevE.101.053104

[44] M.A. Alves, F.T. Pinho, P.J. Oliveira, Study of steady pipe and channel flows of a single-mode Phan–Thien–Tanner fluid, J. Non-Newtonian Fluid Mech. 101 (2001) 55–76. https://doi.org/10.1016/S0377-0257(01)00159-8

[45] D.C. Tretheway, C.D. Meinhart, Apparent fluid slip at hydrophobic microchannel walls, Phys. Fluids 14 (2002) L9–L12. https://doi.org/10.1063/1.1432696

[46] P. Kaushik, S. Pati, S.K. Som, S. Chakraborty, Hydrodynamic and thermal transport characteristics of swirling flows through microchannels with interfacial slip, Int. J. Heat Mass Transf. 55 (2012) 4359–4365. https://doi.org/10.1016/j.ijheatmasstransfer.2012.04.004

Supplementary Files

This is a list of supplementary files associated with this preprint. Click to download.

- Highlights.docx